

Improving lognormal models for cosmological fields

Henrique S. Xavier^{1,2*}, Filipe B. Abdalla^{2,3} and Benjamin Joachimi²

¹ Instituto de Astronomia, Geofísica e Ciências Atmosféricas, Universidade de São Paulo, Rua do Matão, 1226, São Paulo, SP 05508-090, Brazil

² Department of Physics & Astronomy, University College London, 3rd Floor, 132 Hampstead Road, London NW1 2PS, UK

³ Department of Physics and Electronics, Rhodes University, PO Box 94, Grahamstown, 6140, South Africa

18 July 2017

ABSTRACT

It is common practice in cosmology to model large-scale structure observables as lognormal random fields, and this approach has been successfully applied in the past to the matter density and weak lensing convergence fields separately. We argue that this approach has fundamental limitations which prevent its use for jointly modelling these two fields since the lognormal distribution's shape can prevent certain correlations to be attainable. Given the need of ongoing and future large-scale structure surveys for fast joint simulations of clustering and weak lensing, we propose two ways of overcoming these limitations. The first approach slightly distorts the power spectra of the fields using one of two algorithms that minimises either the absolute or the fractional distortions. The second one is by obtaining more accurate convergence marginal distributions, for which we provide a fitting function, by integrating the lognormal density along the line of sight. The latter approach also provides a way to determine directly from theory the skewness of the convergence distribution and, therefore, the parameters for a lognormal fit. We present the public code *Full-sky Lognormal Astro-fields Simulation Kit* (FLASK) which can make tomographic realisations on the sphere of an arbitrary number of correlated lognormal or Gaussian random fields by applying either of the two proposed solutions, and show that it can create joint simulations of clustering and lensing with sub-per-cent accuracy over relevant angular scales and redshift ranges.

Key words: methods: statistical – gravitational lensing: weak – large-scale structure of Universe

1 INTRODUCTION

One important concept used in cosmology is the random field, i.e. a field defined in space V whose value $F(\mathbf{r})$ at position \mathbf{r} is a random variable (see Peebles 1993). Examples of cosmological random fields are the matter density, matter velocity, CMB temperature fluctuations and polarisation, gravitational lensing convergence and shear fields. The full characterisation of a random field could be obtained with the specification of the joint probability density function (PDF) $f_{\text{joint}}(\mathbf{F})$ for $\mathbf{F} = \{F(\mathbf{r}) \mid \mathbf{r} \in V\}$.

A common and simple approximation used is to assume that $f_{\text{joint}}(\mathbf{F})$ is a multivariate Gaussian distribution. In this scenario, all marginal distributions – the PDFs $f[F(\mathbf{r})]$ for any particular \mathbf{r} – are Gaussians and f_{joint} is fully characterised by the mean vector $\boldsymbol{\mu} = \{\mu(\mathbf{r}) \mid \mathbf{r} \in V\}$ (which in cosmology is generally zero) and the covariance matrix $\mathbf{C}(\mathbf{r}, \mathbf{r}')$. Within this model it is possible to fully characterise $f_{\text{joint}}(\mathbf{F})$ (and therefore the random field) by constraining $\mathbf{C}(\mathbf{r}, \mathbf{r}')$, and probably the simplest way to do this is to measure the field's correlation function $\xi_F(\mathbf{r}, \mathbf{r}')$ [which for a zero mean Gaussian field is actually equal to $\mathbf{C}(\mathbf{r}, \mathbf{r}')$] or

its counterpart in Fourier or harmonic space. Further simplifications come from the statistical homogeneity of the Universe, which makes $\xi_F(\mathbf{r}, \mathbf{r}') = \xi_F(\mathbf{r} - \mathbf{r}')$, and statistical isotropy, which leads to $\xi_F(\mathbf{r} - \mathbf{r}') = \xi_F(|\mathbf{r} - \mathbf{r}'|)$.

In some cases the multivariate Gaussian distribution is clearly not a good approximation. The matter density contrast $\delta(\mathbf{r}) = [\rho(\mathbf{r}) - \bar{\rho}]/\bar{\rho}$, where $\rho(\mathbf{r})$ is the density at position \mathbf{r} and $\bar{\rho}$ its average, and the lensing convergence $\kappa(\mathbf{r})$ marginal distributions have hard lower limits which are not obeyed by Gaussian distributions and they show significant skewnesses and heavy tails at large values. A better approximation for $f_{\text{joint}}(\mathbf{F})$ is the multivariate shifted lognormal distribution (Coles & Jones 1991; Taruya et al. 2002; Hilbert et al. 2011).

If a set of variables follows a multivariate lognormal distribution, this means that their logarithms follow a multivariate Gaussian distribution. The “shifted” term expresses simply that the distribution is translated around the space populated by the variables (see Sec. 2.1 for details). Even though this model introduces the shifts as extra parameters, they are in principle fixed by theory so a measurement of $\xi_F(\mathbf{r}, \mathbf{r}')$ would also fully determine $f_{\text{joint}}(\mathbf{F})$; if the shifts are left to vary, an extra measurement like the marginals' skewnesses are needed. This model has been

* E-mail: hsxavier@if.usp.br

extensively used for representing both the matter/galaxy densities (Coles & Jones 1991; Chiang et al. 2013) and the convergence field (Taruya et al. 2002; Hilbert et al. 2011), and it was shown to provide a better approximation than the multivariate Gaussian, but it was also shown to depart from observational results and numerical simulations (Kofman et al. 1994; Bernardeau & Kofman 1995; Kayo et al. 2001; Joachimi et al. 2011; Neyrinck 2011; Seo et al. 2012). One of its main uses is to quickly simulate large-scale structure (LSS) observations to estimate measurement errors (Chiang et al. 2013; Alonso et al. 2015) and to test pipelines and estimators (e.g. Beutler et al. 2014), all crucial steps for LSS surveys like the Dark Energy Survey¹ (DES; DES Collaboration 2005), *Euclid*² (Lumb et al. 2009), the Javalambre Physics of the accelerating universe Astrophysical Survey³ (J-PAS; Benítez et al. 2014), the Large Synoptic Survey Telescope⁴ (LSST; LSST collaboration 2009) and the *Wide-field Infrared Survey Explorer*⁵ (WISE; Wright 2010). Note that all these projects will cover large portions of the sky (from 5000 deg² onwards) and many will reach redshifts of one or more.

In this paper we highlight an intrinsic limitation of lognormal variables mostly unknown by the astrophysical community that might irretrievably prevent its use for modelling simultaneous measurements of galaxy density and weak lensing. This limitation comes from three combined facts: (a) the relation between two lognormal variables with different skewnesses is non-linear; (b) in cosmology the widely used measure for dependence between two variables is the Pearson correlation coefficient which works well only for linearly related variables; (c) the assumption that the density is lognormally distributed means that the convergence is not. We propose two different approaches to deal with this issue: distorting either the density and convergence fields’ auto- and cross-power spectra or the convergence marginal distributions (away from lognormals, making it in fact more realistic). We also present the open source code entitled Full-sky Lognormal Astro-fields Simulation Kit (FLASK)⁶, capable of creating tomographic Gaussian and lognormal realisations of multiple correlated fields (multiple tracers, weak lensing convergence, etc.) on the full sky – using spherical coordinates – and of applying the two corrections suggested above.

This paper is organised as follows: an introduction to lognormal variables is given in Sec. 2.1, then in Sec. 2.2 we show how items (a) and (b) referred to above combine in a way to restrict the covariance matrices realisable by lognormal variables, while in Sec. 2.3 we analyse how this restriction translates into the harmonic space (i.e. the computation of angular power spectra). We then show in Sec. 3 that the density lognormality assumption leads to a non-lognormal distribution for the weak lensing convergence field, which might cause the lognormal model failure. Nevertheless, using this assumption we derive an analytical way of computing the convergence lognormal shift parameter which can be used to model the convergence field alone without resorting to ray-tracing measurements in N -body simulations; in this section we also present a fitting function for the convergence distribution to better describe its deviations from the lognormal model. Sec. 4 details the two solutions to the modelling problem, already hinted by the previous sections: distorting the power spectra or using a theoretically

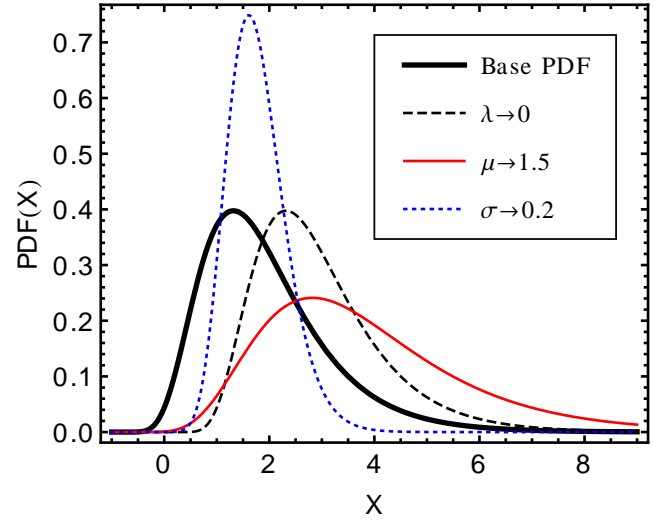


Figure 1. Examples of lognormal probability density functions (PDFs). The base distribution (presented in thick black line) has the parameters $\mu = 1$, $\sigma = 0.4$ and $\lambda = 1$. The remaining curves are obtained by changing the value of one parameter at a time. The λ change to zero translates the curve to the right (dashed black line), the μ change to 1.5 stretches the curve to the right (solid red line) and the decrease in σ to 0.2 changes the distribution’s shape, making it less skewed and closer to a Gaussian (dotted blue line).

consistent distribution for the convergence. Our code FLASK is described in Sec. 5, with an overview given in Sec. 5.1 and the details in Sec. 5.2. We conclude and summarise our work in Sec. 6.

2 LOGNORMAL VARIABLES

2.1 Definition and properties

Given a set of variables Z_i following a multivariate Gaussian distribution with mean vector elements μ_i and covariance matrix elements ξ_g^{ij} , we call the random variables:

$$X_i = e^{Z_i - \lambda_i} \quad (1)$$

multivariate shifted lognormal variables, or lognormal variables for short in this paper. The parameters λ_i are called “shifts” by Hilbert et al. (2011) while $-\lambda_i$ are called “minimum values” by Taruya et al. (2002) and “thresholds” in the statistics literature (e.g. Crow & Shimizu 1988). A single lognormal variable is then fully described by three parameters: the shift λ_i (which acts as a location parameter), the associated Gaussian variable’s mean μ_i (which acts as a scaling parameter) and the associated Gaussian variable’s variance $\sigma_i^2 \equiv \xi_g^{ii}$ (which acts as a shape parameter). Since it possesses one extra parameter in comparison to Gaussian variables, it is more flexible than the latter. In fact, it tends to the Gaussian case as $\sigma_i^2 \rightarrow 0$. Fig. 1 presents examples of the effects on the PDF of changing the distribution’s parameters.

The relations between the correlation function of lognormal variables and their parameters μ_i , λ_i and ξ_g^{ij} have been presented in the astrophysical literature for the case $\lambda_i = 0$ by Coles & Jones (1991) and for $\langle X_i \rangle = 0$ and $\lambda_i = \lambda$ by Hilbert et al. (2011). Here we generalise their results for multiple arbitrary shifts λ_i and expected values (i.e. statistical ensemble averages) $\langle X_i \rangle$.

The mean value $\langle X_i \rangle$ of a lognormal variable X_i can be ob-

¹ <http://www.darkenergysurvey.org>

² <http://www.euclid-ec.org>

³ <http://j-pas.org>

⁴ <http://www.lsst.org>

⁵ <http://wise.ssl.berkeley.edu>

⁶ <http://www.astro.iag.usp.br/~flask>

tained from Eq. 1 by expanding the exponential as an infinite series:

$$\langle e^{Z_i} \rangle = e^{\mu_i} \langle e^{Z_i - \mu_i} \rangle = e^{\mu_i} \sum_{n=0}^{\infty} \frac{\langle (Z_i - \mu_i)^n \rangle}{n!} \quad (2)$$

and remembering that the Gaussian central moments $\langle (Z_i - \mu_i)^n \rangle$ follow the relation

$$\langle (Z_i - \mu_i)^n \rangle = \begin{cases} 0, & \text{if } n \text{ is odd,} \\ \frac{n!}{(n/2)!} \left(\frac{\sigma_i^2}{2} \right)^{n/2}, & \text{if } n \text{ is even.} \end{cases} \quad (3)$$

By inserting Eq. 3 into Eq. 2 and defining a new summation index $m \equiv n/2$, we get:

$$\langle X_i \rangle = e^{\mu_i + \frac{\sigma_i^2}{2}} - \lambda_i. \quad (4)$$

To derive the relation between the lognormal and associated Gaussian covariances ξ_{\ln}^{ij} and ξ_g^{ij} , we can write Z_i as a sum of zero-mean independent Gaussian variables g_n , e.g. $Z_1 = \mu_1 + g_1 + g_0$ and $Z_2 = \mu_2 + g_2 + g_0$ such that $\langle (Z_1 - \mu_1)(Z_2 - \mu_2) \rangle = \langle g_0^2 \rangle$. This allows us to treat the expectation value $\langle e^{Z_1 - \mu_1} e^{Z_2 - \mu_2} \rangle$ as a product of independent terms:

$$\langle e^{Z_1 - \mu_1} e^{Z_2 - \mu_2} \rangle = \langle e^{g_1} \rangle \langle e^{g_2} \rangle \langle e^{2g_0} \rangle \quad (5)$$

to which we can apply the same procedure used to derive Eq. 4, leading to:

$$\xi_{\ln}^{ij} \equiv \langle X_i X_j \rangle - \langle X_i \rangle \langle X_j \rangle = \alpha_i \alpha_j (e^{\xi_g^{ij}} - 1), \quad (6)$$

$$\xi_g^{ij} = \ln \left(\frac{\xi_{\ln}^{ij}}{\alpha_i \alpha_j} + 1 \right), \quad (7)$$

where $\alpha_i \equiv \langle X_i \rangle + \lambda_i > 0$. Again the same method can be used to derive a relation for the three-point correlation function of lognormal variables:

$$\begin{aligned} \xi_{\ln}^{ijk} &\equiv \langle (X_i - \langle X_i \rangle)(X_j - \langle X_j \rangle)(X_k - \langle X_k \rangle) \rangle = \\ &= \frac{\xi_{\ln}^{ij} \xi_{\ln}^{jk} \xi_{\ln}^{ki}}{\alpha_i \alpha_j \alpha_k} + \frac{\xi_{\ln}^{ji} \xi_{\ln}^{ik}}{\alpha_i} + \frac{\xi_{\ln}^{ij} \xi_{\ln}^{jk}}{\alpha_j} + \frac{\xi_{\ln}^{ik} \xi_{\ln}^{kj}}{\alpha_k}. \end{aligned} \quad (8)$$

By setting all indices in Eqs. 6 and 8 to the same value, we get relations for the variance v_i and skewness γ_i of a lognormal variable:

$$v_i \equiv \langle X_i^2 \rangle - \langle X_i \rangle^2 = \alpha_i^2 (e^{\sigma_i^2} - 1), \quad (9)$$

$$\gamma_i \equiv \frac{\langle (X_i - \langle X_i \rangle)^3 \rangle}{v_i^{3/2}} = \frac{\sqrt{v_i}}{\alpha_i} \left(\frac{v_i}{\alpha_i^2} + 3 \right). \quad (10)$$

The equation above can be inverted to obtain α_i as a function of γ_i and v_i ; although in principle Eq. 10 admits more than one α_i as a solution, only one of them is real as the relation is monotonic. The shift parameter λ_i can then be written in terms of the variable's mean, variance and skewness:

$$\lambda_i = \frac{\sqrt{v_i}}{\gamma_i} \left[1 + y(\gamma_i) + \frac{1}{y(\gamma_i)} \right] - \langle X_i \rangle, \quad (11)$$

$$y(\gamma) \equiv \sqrt[3]{\frac{2 + \gamma^2 + \gamma\sqrt{4 + \gamma^2}}{2}}. \quad (12)$$

Once we have computed λ_i , we can get the remaining parameters of the lognormal distribution that possess the specified first three moments by inverting Eqs. 4 and 9:

$$\mu_i = \ln \left(\frac{\alpha_i^2}{\sqrt{\alpha_i^2 + v_i}} \right), \quad (13)$$

$$\sigma_i = \sqrt{\ln \left(1 + \frac{v_i}{\alpha_i^2} \right)}. \quad (14)$$

This provides us with a method to fit a lognormal distribution to a dataset that exactly reproduces its mean, variance and skewness.

2.2 Intrinsic limitations of multivariate lognormals

To expose the fundamental limitations that lognormal variables face when modelling correlated data, consider a toy model consisting of only two variables. We can use Eq. 6 to build a relation between the Pearson correlation coefficients of the lognormal variables, ρ_{\ln} , and that of their associated Gaussian variables, ρ_g :

$$\rho_{\ln} = \frac{e^{\rho_g \sigma_1 \sigma_2} - 1}{\sqrt{(e^{\sigma_1^2} - 1)(e^{\sigma_2^2} - 1)}}, \quad (15)$$

where σ_1^2 and σ_2^2 are the variances of the Gaussian variables and serve as shape parameters (which fully determines the skewness) of the lognormal distributions. The relation above is presented in Fig. 2 for different values of σ_1^2 and σ_2^2 , where it is possible to note that even perfectly correlated Gaussian variables ($\rho_g = 1$) may not result in perfectly correlated lognormal variables. This happens because one cannot impose a linear relation between two variables X and Y if their distributions have different shapes (e.g. different skewnesses) since such a relation only corresponds to shifting and rescaling one distribution to match the other (see Fig. 3). These limits on the Pearson correlation coefficient can be written in terms of the parameters of lognormal variables:

$$\frac{\alpha_1 \alpha_2}{\sqrt{v_1 v_2}} (e^{-L} - 1) < \rho_{\ln} < \frac{\alpha_1 \alpha_2}{\sqrt{v_1 v_2}} (e^L - 1), \text{ with} \quad (16)$$

$$L \equiv \sqrt{\ln \left(\frac{v_1}{\alpha_1^2} + 1 \right) \ln \left(\frac{v_2}{\alpha_2^2} + 1 \right)}. \quad (17)$$

A more rigorous and general (but also complex) proof of the correlation limits above can be obtained from the use of copulas (Nelsen 2006): any multivariate distribution can be described by a copula – a multidimensional function that alone specifies the variables' inter-dependences – together with the one-dimensional marginal distributions of these variables. Copulas are useful because the dependence between the random variables becomes detached from their marginal distributions. The Fréchet–Hoeffding theorem states that all copulas are limited by specific functions W and M called *lower* and *upper Fréchet–Hoeffding bounds*. It is then possible to derive Eq. 16 by setting the two-dimensional copula to W and M and calculating the resulting correlations (see also Denuit & Dhaene 2003).

Suppose now that one ignores the limits above and assigns to

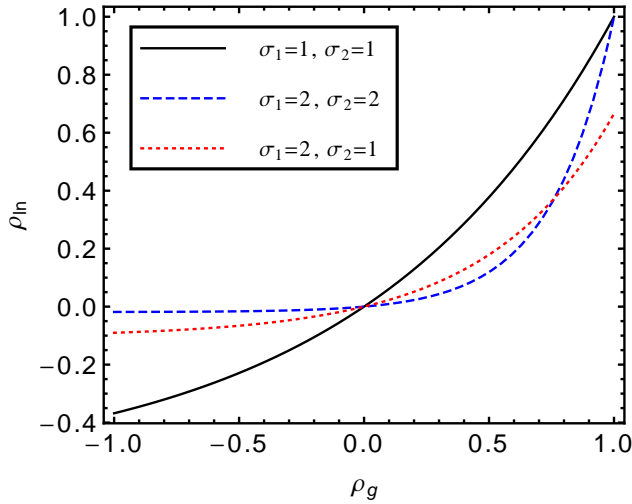


Figure 2. Relationship between the correlation ρ_g of two Gaussian variables and the correlation ρ_{ln} of their associated lognormal variables. The amount of Pearson correlation and anti-correlation of lognormal variables is smaller than the correlation of their Gaussian counterparts and the relation depends on the Gaussian variances σ_1^2 and σ_2^2 .

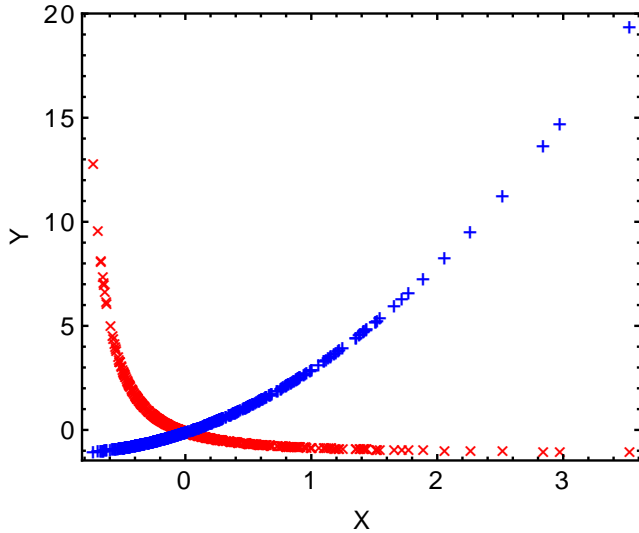


Figure 3. Each marker shows 400 realisations of fully dependent lognormal random variables X and Y , that is, $\ln(Y+1) = -2\ln(X+1)$, shown as red crosses, and $\ln(Y+1) = 2\ln(X+1)$, shown as blue plus signs. Even though their associated Gaussian variables are completely anti-correlated and completely correlated, respectively, the absolute values of their Pearson correlations are smaller than one: 0.58 and 0.94. This happens because the relation between them is non-linear.

a pair of lognormal variables a valid (i.e. positive-definite) covariance matrix but that violates Eq. 16. By using Eq. 7 one would find $|\rho_g| > 1$, which for a 2×2 covariance matrix corresponds to being invalid (i.e. non-positive-definite).⁷ Since lognormal variables are associated to Gaussian variables by definition, the non-positive-definiteness of the Gaussian variables' covariance matrix shows that such lognormal variables cannot exist. In other words, a covariance matrix for lognormal variables is only valid if both itself

and its Gaussian counterpart are positive-definite.⁸ This statement can be extended to covariance matrices of arbitrary size; this is important because, when dealing with more than two variables, the condition set by Eq. 16 is necessary but not sufficient.

As an example of what may happen in more complex cases, imagine there are three lognormal variables with $\alpha_1 = 1$ and $\alpha_2 = \alpha_3 = 0.1$ that follow the covariance matrix below on the left:

$$\begin{pmatrix} 1 & 0.45 & 0.45 \\ 0.45 & 1 & 0.40 \\ 0.45 & 0.40 & 1 \end{pmatrix} \rightarrow \begin{pmatrix} 1 & 0.95 & 0.95 \\ 0.95 & 1 & 0.80 \\ 0.95 & 0.80 & 1 \end{pmatrix}. \quad (18)$$

This positive-definite (and seemingly innocent) covariance matrix hides the fact that the dependence between the first variable and the two others is very strong (the maximum correlation allowed by the difference in the shape of their distributions is ~ 0.50) whereas the dependence between the last two variables is not strong enough to be compatible with the former (since they have the same shape, their maximum correlation is 1). Indeed, the correlation matrix of the associated Gaussian variables (right-hand side of Eq. 18) is non-positive-definite.

The limitations over three or more lognormal variables appear even when the one-dimensional marginals are exactly the same. Fig. 4 shows that the Gaussian covariances serve as shape parameters for the multivariate lognormal distribution just as the Gaussian variances σ_i do due to the non-linearity of the transformation. The shape of the distribution can be such that projections on two-dimensional spaces might give the impression that tighter correlations are possible when they are not.

Another way to deduce the connection between lognormal variables and their Gaussian counterparts covariance matrix is the following:

- (i) *Fact:* lognormal variables always have, by definition, Gaussian variables associated to them;
- (ii) *Fact:* any set of N random variables must have a valid $N \times N$ covariance matrix associated to it;
- (iii) *Hypothesis:* $\{X_1, \dots, X_N\}$ is a set of multivariate lognormal variables and it has the covariance matrix \mathbf{C}_{ln} ;
- (iv) *Consequence from (i):* there is a set $\{Z_1, \dots, Z_N\}$ of Gaussian variables related to $\{X_1, \dots, X_N\}$ by Eq. 1;
- (v) *Consequence from (ii):* $\{Z_1, \dots, Z_N\}$ have a valid covariance matrix \mathbf{C}_g that can be obtained from Eq. 6.

If our final conclusion (v) is not true, our hypothesis (iii) must be false, that is, either $\{X_1, \dots, X_N\}$ are not multivariate lognormal variables or they do not follow \mathbf{C}_{ln} . Trying to enforce both at the same time would be like requesting two different angles from an equilateral triangle. Note that the relation between \mathbf{C}_{ln} and \mathbf{C}_g depends on the full multi-dimensional PDF of $\{X_1, \dots, X_N\}$ so although it might not be a multivariate lognormal it can retain, in principle, marginal lognormal distributions.

2.3 Limitations in harmonic space

A collection of 3D isotropic random fields can be described by a set of angular correlation functions $\xi^{ij}(\theta)$ for fields and redshift slices specified by the indices i and j . These correlation functions can be expressed in terms of angular power spectra $C^{ij}(\ell)$ through the relations (Durrer 2008):

⁷ Assuming that the diagonal terms are positive.

⁸ Since the relation between Gaussian variables is always linear, their Pearson correlation actually reflects the degree of dependence between them.

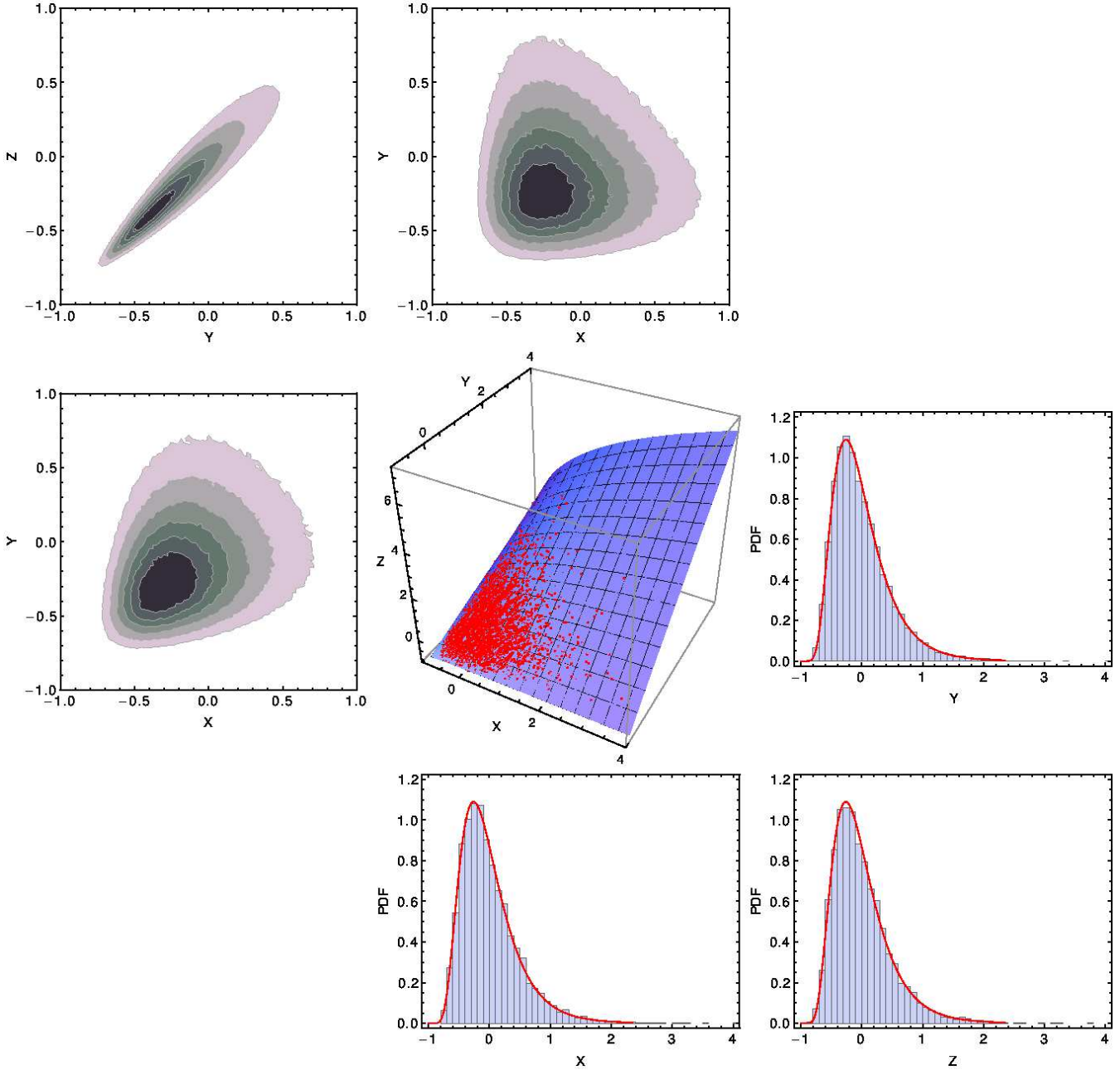


Figure 4. The plots show the three 1D marginal distributions (bottom right corner), three 2D marginal distributions (top left corner) and the scatter plot (centre) of three correlated lognormal random variables (yellow dots). The variables have a strong non-linear dependence that confines them into a space of lower dimensionality (the curved surface shown in the centre plot) and therefore stronger Pearson correlations might not be achievable, even though the 2D marginals do not indicate that and the 1D marginals have exactly the same shape. The correlations between the variables (together with their variances and minimum values) determine the 3D distribution's shape.

$$C^{ij}(\ell) = 2\pi \int_0^\pi \xi^{ij}(\theta) P_\ell(\cos \theta) \sin \theta d\theta, \quad (19)$$

$$\xi^{ij}(\theta) = \frac{1}{4\pi} \sum_{\ell=0}^{\infty} (2\ell+1) C^{ij}(\ell) P_\ell(\cos \theta), \quad (20)$$

where $P_\ell(\mu)$ are Legendre polynomials.

If the fields in question follow lognormal distributions in real space, the relation between the angular power spectra $C_{\ln}^{ij}(\ell)$ and

$C_g^{ij}(\ell)$ that describe the lognormal fields and their associated Gaussian counterparts, respectively, is

$$C_g^{ij}(\ell) = 2\pi \int_{-1}^1 \ln \left[\sum_{\ell'=0}^{\infty} \frac{(2\ell'+1)}{4\pi} \frac{C_{\ln}^{ij}(\ell')}{\alpha_i \alpha_j} P_{\ell'}(\mu) + 1 \right] P_\ell(\mu) d\mu. \quad (21)$$

Although the relation above is not as direct as the one in real space (see Eq. 7), it takes advantage of isotropy to make each multipole independent of one another and reduce the dimensionality of the covariance matrices to the number of fields and redshift slices spec-

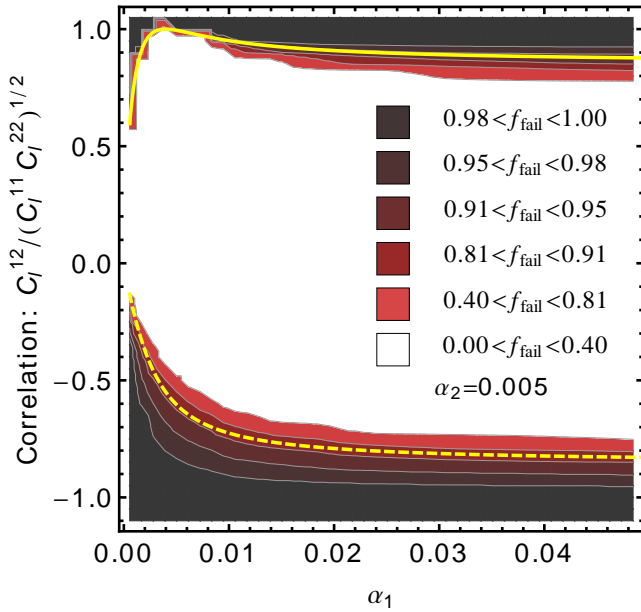


Figure 5. The dashed and solid thick yellow lines show the lower and upper correlation limits according to Eq. 16; we set $\alpha_2 = 0.005$ and the variances v_1 and v_2 were computed using Eq. 20 with $i = j$ and $\theta = 0$. The shaded regions are coloured according to the fraction f_{fail} of $C_{\text{ln}}^{ij}(\ell)$ in the range $2 \leq \ell \leq 5000$ that failed to result in positive-definite $C_{\text{g}}^{ij}(\ell)$ (see the text). In harmonic space, the correlation limits get blurred but retain approximately the same form.

ified by i and j . In other words, for each ℓ we have an independent covariance matrix $\mathbf{C}(\ell)$ with elements $C^{ij}(\ell)$.

It is difficult to derive analytically how the restriction described in Sec. 2.2 affects the relation between $C_{\text{ln}}^{ij}(\ell)$ and $C_{\text{g}}^{ij}(\ell)$: given it is local in real space, the relation becomes non-local in harmonic space, i.e. $C_{\text{g}}^{ij}(\ell)$ relates to a combination of $C_{\text{ln}}^{ij}(\ell')$ with different ℓ' ; moreover, the multipoles described by $C_{\text{ln}}^{ij}(\ell)$ are not themselves lognormal. However, a highly correlated field in real space should be highly correlated in harmonic space as well and therefore the conditions set in Sec. 2.2 cannot be completely avoided. This is shown in Fig. 5.

To draw the shaded regions in Fig. 5 we first computed the convergence auto- and cross-power spectra for sources inside 0.1-wide top-hat redshift bins centred at $z_1 = 0.5$ and $z_2 = 0.6$ using CLASS⁹ (Blas et al. 2011; Dio et al. 2013) and a flat Λ CDM model. These $C_{\text{ln}}^{ij}(\ell)$ were transformed to $C_{\text{g}}^{ij}(\ell)$ using Eq. 21 – implemented by FLASK – and α_i obtained by Hilbert et al. (2011) using ray tracing through N -body simulations. For each ℓ we built a 2×2 covariance matrix $\mathbf{C}_{\text{g}}(\ell)$ which was tested for positive-definiteness. To probe the whole parameter space in Fig. 5 we repeated this process several times after rescaling the cross power spectrum and changing α_1 .

The final message of Fig. 5 is that the limitations described in Sec. 2.2 manifest themselves in harmonic space and can indeed prevent the realisation of multipoles of lognormal fields, showing in these cases that the proposed fields cannot exist. Moreover, this seems to be the only relevant process affecting the positive-definiteness of $\mathbf{C}_{\text{g}}(\ell)$ – at least in the simple example shown and aside from much smaller numerical errors.

3 LOGNORMAL LARGE-SCALE STRUCTURE MODELS

3.1 Quantifying the lognormal failure and distorting $C^{ij}(\ell)$

We investigated if the limitations referred to in the previous section manifest themselves in the density and convergence fields. We described the projected matter density contrast δ inside redshift bins and the weak lensing convergence κ for sources inside those bins as multivariate lognormal variables that obey a set of $C_{\text{ln}}^{ij}(\ell)$ with $i = \{\delta(z_1), \dots, \delta(z_n), \kappa(z_1), \dots, \kappa(z_n)\}$ and inferred the model’s validity by checking if the matrices $\mathbf{C}_{\text{g}}(\ell)$ with elements given by Eq. 21 were positive-definite.

When a matrix $\mathbf{C}_{\text{g}}(\ell)$ turned out to be non-positive-definite, we quantified the degree of “non-positive-definiteness” by computing the fractional change in the matrix elements needed to make it positive-definite. For that we used a multi-dimensional gradient to minimise the sum of the absolute values of the negative eigenvalues: by computing the change in the negative eigenvalues given a small fractional change in each one of the $N \times N$ matrix elements we found a preferential direction in this $N \times N$ -dimensional space to distort the matrix and applied a small change in this direction; we repeated this process until all eigenvalues were positive. Another method to regularise a covariance matrix is to perform an eigendecomposition of the matrix $[\mathbf{C}_{\text{g}} = \mathbf{Q}\mathbf{\Lambda}\mathbf{Q}^{-1}]$, where \mathbf{Q} is a matrix formed by the eigenvectors of \mathbf{C}_{g} and $\mathbf{\Lambda}$ is a diagonal matrix formed by \mathbf{C}_{g} eigenvalues and set the negative eigenvalues to zero. However, this method results in minimal absolute rather than minimal fractional changes; more specifically, it is guaranteed to minimise the Frobenius norm – i.e. the matrix elements’ quadratic sum – of the difference between the original and regularised matrices (Higham 1988). We confirmed that the fractional change obtained by our method is indeed smaller than the one obtained from the latter, and that they both result in fractional changes of similar magnitude for $C_{\text{g}}^{ij}(\ell)$ not too close to zero. Both regularisation methods can be performed by FLASK. The regularised $C_{\text{g}}^{ij}(\ell)$ can be transformed back into $C_{\text{ln}}^{ij}(\ell)$ to give a set of angular power spectra that would not fail to represent lognormal fields.

High fractional changes are needed when trying to model both density and convergence as lognormal fields. Broadly speaking the amount of $C_{\text{ln}}^{ij}(\ell)$ distortion required to make $C_{\text{g}}^{ij}(\ell)$ positive-definite increases with ℓ and with the number of redshift bins, and is higher for the non-linear power spectra computed by HALOFIT (Smith et al. 2003; Takahashi et al. 2012) and when low-redshift bins are included: with the closest bin centred at $z = 0.3$, the required amount of change goes from $\sim 1.2\%$ ($\sim 4\%$) for 3 bins to $\sim 8\%$ ($\sim 20\%$) for 20 bins when using linear (non-linear) power spectra. Other parameters have a smaller impact on the fractional changes. As Fig. 6 shows, changes affect mainly the high multipoles and are much larger than the numerical precision expected for these operations (see below).

To ensure that the results presented in Fig. 6 were not caused by numerical inaccuracies, we used both CLASS and CAMB SOURCES¹⁰ (Challinor & Lewis 2011) to generate the required $C_{\text{ln}}^{ij}(\ell)$ under a variety of precision settings and performed the transformation described in Eq. 21 using two different methods under two different programming languages. Our main method (implemented in FLASK) was built in C and used the discrete Legendre transform coded in S2KIT¹¹ (Kostelec et al. 2000) to go back and forth into harmonic space, while our second method used the func-

⁹ <http://class-code.net>

¹⁰ <http://camb.info/sources>

¹¹ <http://www.cs.dartmouth.edu/~geelong/sphere>

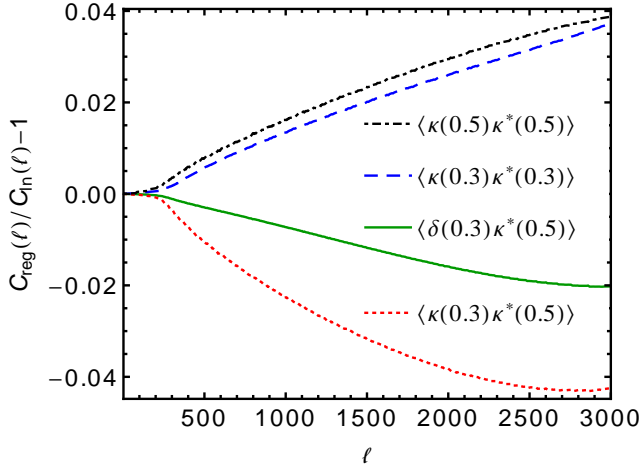


Figure 6. Four highest fractional differences between the original angular power spectra $C_{\text{in}}^{ij}(\ell)$ and the regularised one $C_{\text{reg}}^{ij}(\ell)$ when modelling density and convergence at three redshift bins. The difference increases with ℓ up to $\ell = 3000$. In general the diagonal terms [auto- $C(\ell)$ s] are increased while off-diagonal terms [cross- $C(\ell)$ s for different redshift bins] are decreased, reducing the correlation between redshift slices.

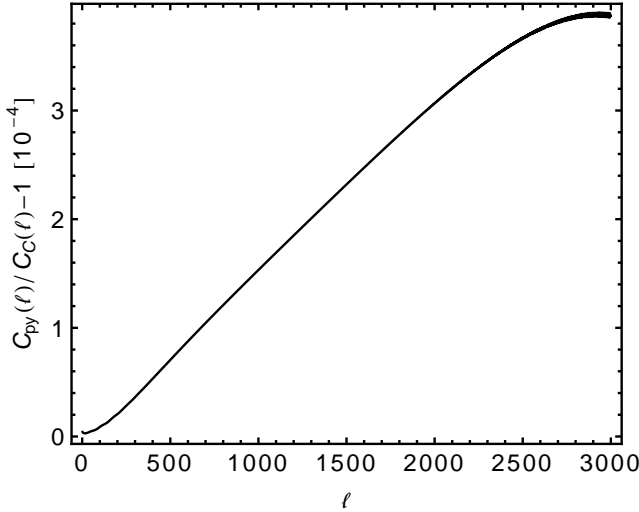


Figure 7. Highest fractional difference between $C_g^{ij}(\ell)$ computed with PYTHON and C routines for density and convergence fields at three different redshift bins (total of 21 power spectra). The PYTHON routine diverges at $\ell \sim \ell_{\text{max}}$ (while the C routine does not) so we set $\ell_{\text{max}} = 7000$. Numerical fractional errors on the transformation given by Eq. 21 are expected to be smaller than 4×10^{-4} up to $\ell = 3000$, specially for the routine in C.

tions LEGVAL and LEGFIT in PYTHON’s NUMPY package. Fig. 7 shows that numerical fractional errors are expected to remain below 4×10^{-4} . We also confirmed the behaviour of our results for Gaussian and top-hat redshift bins of different widths, with and without different contributions included in the matter density distribution (redshift space distortions, gravitational lensing, Integrated Sachs–Wolfe effect and gravitational redshift) and with and without non-linear structure given by HALOFIT.

When considering matter density contrast or weak lensing convergence separately – i.e. when modelling one of these fields independently of the other – any need for regularising covariance matrices results in diminute fractional changes, of order 10^{-5} , that

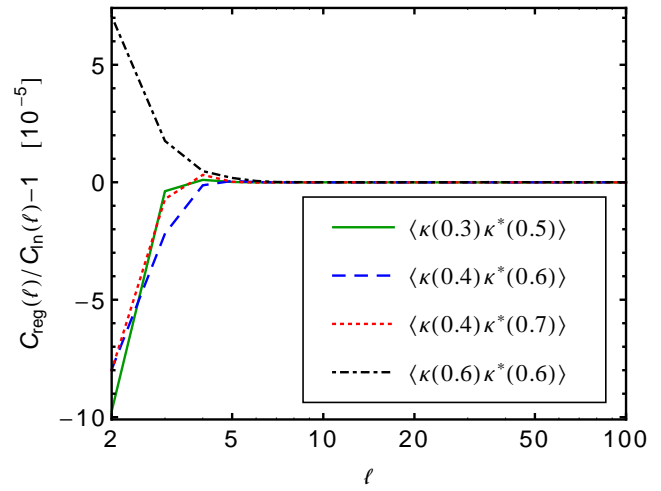


Figure 8. Same as Fig. 8 but for convergence only, computed in 19 redshift bins. The difference is largest at low multipoles; we tested up to $\ell = 3000$. As before, regularisation reduces the correlations between fields and redshift bins.

in general affect low multipoles ($\ell \lesssim 50$). Such small deviations from positive-definiteness might be caused by numerical inaccuracies and, in any case, are too small to be detectable especially at low multipoles where cosmic variance is large. We verified that this pattern is maintained for different matter density contributions portfolio, for the linear and non-linear power spectra, for CLASS and CAMB SOURCES with different precision settings and for various redshift ranges and binning (we tested from 2 to 50 redshift bins in the range $0.3 \lesssim z \lesssim 3.0$). In fact, the CLASS computation of density power spectra never resulted in non-positive-definite covariance matrices $C_g^{ij}(\ell)$. As an example, Fig. 8 shows the four largest fractional differences between the original input $C_{\text{in}}^{ij}(\ell)$ and the regularised ones $C_{\text{reg}}^{ij}(\ell)$ when modelling the convergence in 19 top-hat redshift bins of width $\Delta z = 0.1$ in the range $0.2 < z < 2.0$.

3.2 Density and convergence lognormality inconsistency

A model where both density and convergence are lognormal variables includes by definition an internal inconsistency due to the following connection between the two, which ends encoded in the power spectra: one can compute the convergence $\kappa(\theta, z_s)$ for galaxies at angular position θ and redshift z_s by integrating the matter density contrast $\delta(\theta, z)$ along the line of sight (LoS) (Bartelmann & Schneider 2001, eq. 6.16):

$$\kappa(\theta, z_s) = \int_0^{z_s} K(z, z_s) \delta(\theta, z) dz, \quad (22)$$

$$K(z, z_s) \equiv \frac{3H_0^2 \Omega_m}{2c^2} \frac{f[\chi(z)] f[\chi(z_s) - \chi(z)]}{f[\chi(z_s)]} (1+z) \frac{d\chi}{dz}, \quad (23)$$

where $f(\chi)$ is called *transverse comoving distance*:

$$f(\chi) = \begin{cases} \frac{1}{\sqrt{-\Omega_k}} \frac{c}{H_0} \sin\left(\frac{H_0}{c} \sqrt{-\Omega_k} \chi\right), & \Omega_k < 0, \\ \chi, & \Omega_k = 0, \\ \frac{1}{\sqrt{\Omega_k}} \frac{c}{H_0} \sinh\left(\frac{H_0}{c} \sqrt{\Omega_k} \chi\right), & \Omega_k > 0 \end{cases} \quad (24)$$

and $\chi = \chi(z)$ is the comoving distance, given by

$$\chi(z) = \frac{c}{H_0} \int_0^z \frac{dz'}{E(z')}, \quad (25)$$

$$E(z') = \sqrt{\Omega_m(1+z')^3 + \Omega_k(1+z')^2 + \Omega_{de}(1+z')^{3(1+w)}}. \quad (26)$$

In these equations H_0 is the Hubble's constant, c is the speed of light, Ω_m , Ω_{de} and $\Omega_k = 1 - \Omega_m - \Omega_{de}$ are the total matter, dark energy and curvature density parameters, respectively, and w is the dark energy equation of state. From Eq. 22 we see that if each $\delta(\theta, z)$ is drawn from a lognormal distribution then $\kappa(\theta, z_s)$ is a sum of (correlated) lognormal variables. However, in contrast with Gaussian variables, the sum of lognormal variables is not a lognormal variable itself (see Figs. 10, 11 and 12 and Fenton 1960). Following the reasoning presented in the end of Sec. 2.2, this internal inconsistency might be the cause for the lognormal model failure.

3.3 Modelling convergence alone as a lognormal field

Unfortunately, there is no closed expression for the PDF of a sum of lognormal variables; this is still an active field of study and several approximating formulas have been proposed (Fenton 1960; Schwartz & Yeh 1982; Lam & Le-Ngoc 2007; Li et al. 2011). Nevertheless, assuming that the joint probability distribution for $\delta(\theta, z)$ at different z is a multivariate lognormal distribution – i.e. $\ln[\delta(\theta, z)]$ are drawn from a multivariate Gaussian distribution –, it is possible to compute $\kappa(\theta, z_s)$'s moments using the equations described in Appendix A.

Given that $\langle \delta(\theta, z) \rangle = 0$, we have $\langle \kappa(\theta, z_s) \rangle = 0$ as well. The convergence variance and skewness are:

$$\text{Var}[\kappa(z_s)] = \iint_0^{z_s} K(z_1, z_s) K(z_2, z_s) \xi_{\delta\delta}(z_1, z_2) dz_1 dz_2, \quad (27)$$

$$\begin{aligned} \text{Skew}[\kappa(z_s)] &= \frac{1}{\text{Var}^{3/2}[\kappa(z_s)]} \\ &\iint_0^{z_s} \iint_0^{z_s} K(z_1, z_s) K(z_2, z_s) K(z_3, z_s) [3\xi_{\delta\delta}(z_1, z_2)\xi_{\delta\delta}(z_2, z_3) + \\ &\xi_{\delta\delta}(z_1, z_2)\xi_{\delta\delta}(z_2, z_3)\xi_{\delta\delta}(z_3, z_1)] dz_1 dz_2 dz_3, \end{aligned} \quad (28)$$

respectively, where $\xi_{\delta\delta}(z, z') = \langle \delta(\theta, z)\delta(\theta, z') \rangle$ is the matter density contrast LoS correlation function. Eq. 27 does not provide any new information since the variance is already fixed by the convergence power spectrum. Eq. 28, however, puts a constraint over the convergence distribution's shape; if one wants to approximate the convergence as a lognormal variable, it can be used in conjunction with Eq. 11 to specify the distribution's shift parameter λ_i directly from theory. This is useful since previous methods for determining λ_i relied on computationally expensive ray tracing through N -body simulations (e.g. Taruya et al. 2002; Hilbert et al. 2011). Another alternative method for computing lensing PDFs is given by Kainulainen & Marra (2011).

To verify these conclusions numerically, we used FLASK to create 12.5 million lognormal realisations of the LoS matter density in 41 top-hat redshift bins of width $\Delta z = 0.05$ in the range $0.05 < z < 2.10$ and to obtain the convergence at $z = 2.10$ for

Statistic	Numerical	Theory
Mean	3.27×10^{-6}	0
Std. Dev.	0.02182	0.02189
Skewness	0.513	0.508
Lognormal fit		
μ	-2.063	-2.050
σ	0.1682	0.1665
λ	0.1288	0.1306

Table 1. The top part shows the mean, standard deviation and skewness of the convergence distribution obtained through density LoS integration (middle column) and the expected values from theory (0 and those given by Eqs. 27 and 28, last column). The bottom part shows the lognormal distribution parameters that would reproduce the statistics above.

each realisation using Eq. 22. We then measured the statistics of the convergence sample and compared with the values expected from theory. As Table 1 shows, they all match to 1% or better. Using Eqs. 11, 13 and 14 we can compute the parameters of the lognormal distribution that would satisfy such statistics; these parameters are shown in the bottom part of Table 1.

Fig. 9 shows that the theoretical parameters from Table 1 – chosen to reproduce the first three moments of the distribution – indeed provide a good fit for the convergence derived as a sum of correlated lognormal variables. The reproduction however is not perfect as can be seen in Fig. 10. A similar analysis was performed for two-dimensional distributions and the results are presented in Figs. 11 and 12, where we see that the disagreement between the simulated distribution and the lognormal model is larger for the convergence–convergence joint distribution. This is reasonable given that, in this case, both one-dimensional marginals were distorted away from the lognormal model. Therefore, we might expect that higher-dimensional convergence distributions will be even less well approximated by the multivariate lognormal model.

At this point it is important to stress that, since convergence is not strictly a lognormal variable, different methods of determining its shift parameter will result in different values. One possible method – which was implemented by Taruya et al. (2002) – is to set the shift parameter as the minimum attainable convergence; in a lognormal density model, this is clearly the convergence for the empty line of sight [Eq. 22 with $\delta(\theta, z) = -1$] which is hard to be extracted from simulations (or observations) given that these consist of finite samples. Another method (implemented by Hilbert et al. 2011) is to perform a least-squares fit to the convergence PDF. Table 2 compares the values obtained from each method when applied to the convergence modelled as a sum of lognormal variables (density LoS integration) and as a lognormal variable itself. While for the lognormal case the methods agree and return the shift specified *a priori* (apart from the minimum value method which suffers from finite sampling), there is no agreement for the other case (which unfortunately is more realistic). This means that the lognormal approximation for the convergence field cannot reproduce every aspect of the distribution and choices have to be made: if one wants to reproduce the convergence skewness, the moment matching method should be used; if one wants to reproduce the PDF shape as close as possible, the least-squares method should be preferred; and so on.

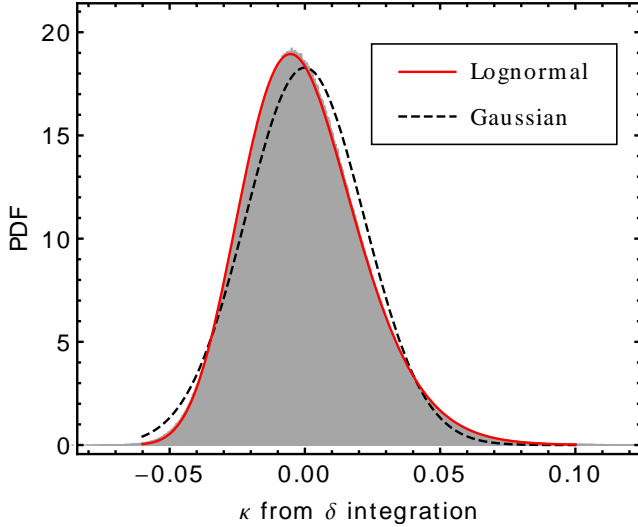


Figure 9. The shaded region is a histogram for the 12.5 million convergences at $z = 2.10$ obtained from lognormal density LoS integration. The black dashed (red solid) line shows a Gaussian (lognormal) distribution that have the same mean and variance (mean, variance and skewness) as the convergence; their parameters are given by the theoretical values in Table 1. The lognormal model performs much better than the Gaussian but significant deviations exist; these are better seen in Fig. 10.

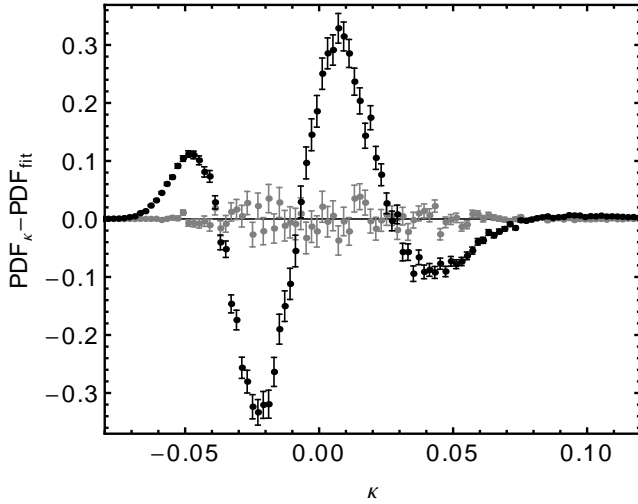


Figure 10. Difference between the PDF of the convergence at $z = 2.10$ obtained from lognormal density LoS integration and the lognormal PDF with the same first three moments (black points); significant deviations exist. The grey points is an example of differences one would get from this moment matching technique if the convergence was indeed lognormal: they would be consistent with zero. The error bars represent the Poisson noise inside each bin.

3.4 Quantifying the deviation from lognormal distribution

To better describe the shape of the convergence 1D marginal distributions obtained by lognormal density LoS integration we used the minimum χ^2 method to fit the following formula to that PDF:

$$f_{ABC}(\kappa) = \frac{1}{\sqrt{2\pi}s} \exp \left\{ -\frac{[ABC'(\kappa) - m]^2}{2s^2} \right\} \frac{dABC'}{d\kappa}, \quad (29)$$

Method	Sum of lognormals	Lognormal
Empty LoS	0.2115	–
True value	–	0.1300
Moment matching	0.1288	0.1306
PDF least square	0.1482	0.1310
Min. value	0.0858	0.0779

Table 2. Possible methods of determining the shift parameter of a lognormal distribution fit to a convergence sample: matching the first three moments; using the least squares method as in Hilbert et al. (2011); selecting the minimum value from the sample as in Taruya et al. (2002). These are applied to a sample of convergences that are sums of correlated lognormal densities (middle column) and to a sample of true lognormal convergences (last column). The results are compared to the true value assigned to the distribution (no such thing for the sum of lognormals) and to the empty line-of-sight value. Comparing the latter with the lognormal sample does not make sense as the latter had the shift parameter set *ad hoc* to match the value obtained for the density LoS integration under the moment matching method.

$$ABC'(\kappa) = \frac{1}{t} \sinh \left\{ \frac{t\kappa_0}{\gamma} \left[\left(\frac{\kappa}{\kappa_0} + 1 \right)^\gamma - 1 \right] \right\}. \quad (30)$$

In the equations above, ABC' is a slightly modified version of the ABC Gaussianization transformation (that is, it transforms variables that follow more general distributions into Gaussian ones; Schuhmann et al. 2016) when its parameters t and γ are restricted to $t > 0$ and $\gamma \neq 0$.¹² The more general κ PDF and the PDF of a Gaussian variable z are related by a simple change of variables: $f(\kappa)d\kappa = G(z)dz$, where $G(z)$ is a Gaussian PDF.

The simulated data used were ~ 3.1 million convergences for sources at each of the redshifts z specified in Table 3, convolved with Gaussian window functions of radius (standard deviation) 1.23 arcmin. These were produced by integrating the lognormal density simulated in 40 equal-width redshifts bins in the range $0.025 < z < 2.025$ (details of this procedure are given in Sec. 4). For each redshift, the convergences were distributed into 500 bins covering the full data range, but when fitting the function given by Eq. 29 we restricted our analysis to the range $\kappa_{\min} < \kappa < \kappa_{\max}$ that does not include bins with zero counts. Together with this range, Table 3 presents for each redshift the $f_{ABC}(\kappa)$ parameters m , s , t , γ and κ_0 that best fit the convergence PDFs, along with the best-fit p -value. In most cases, the p -values indicate that the fits are quite good.

As the redshift increases, the number of density bins that get summed into the convergence increases and its distribution gets closer to a Gaussian due to the central limit theorem, thus making the distribution less complex and requiring less parameters. This is manifested by the strong correlation between γ and κ_0 that grows with redshift up to a point where they diverge and the fits get unstable. To avoid this issue, for redshift 1.075 onwards we fixed γ at the best-fitting value obtained at that redshift. The parameters from Table 3 are also presented in Fig. 13. The resulting $f_{ABC}(\kappa)$ for various redshifts are shown in Fig. 14.

¹² In reality, the $f_{ABC}(\kappa)$ fitting was performed with unrestricted t and γ , but the best fit remained in the $t > 0$ and $\gamma \neq 0$ region. Given that the ABC transformation is a piecewise function, we only show here the $t > 0$ and $\gamma \neq 0$ sub-function.

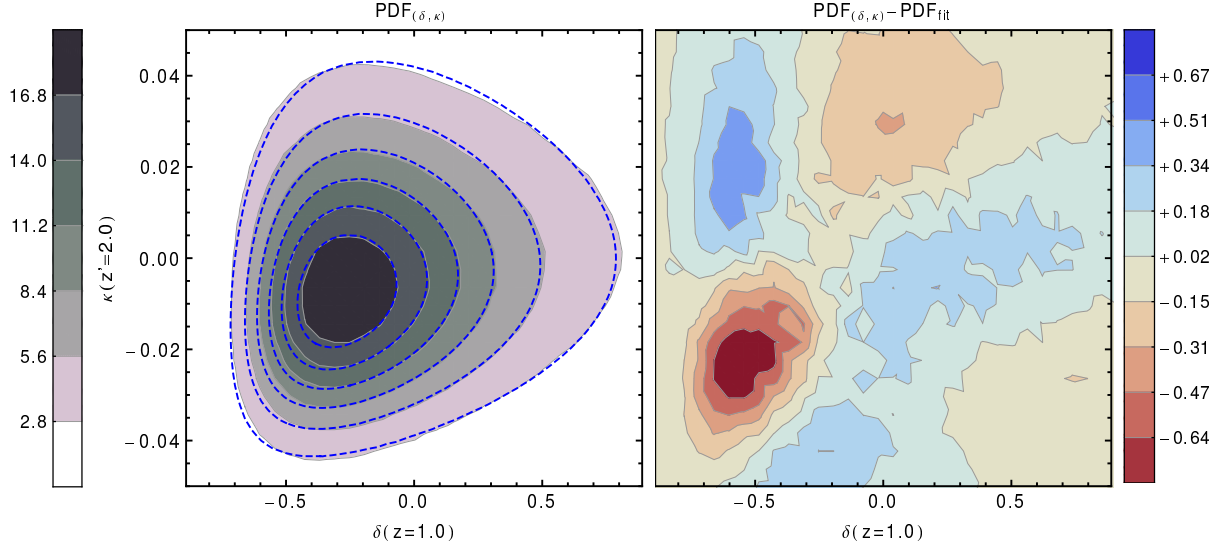


Figure 11. *Left panel:* the shaded regions represent the joint PDF for density contrast $\delta(\theta, z)$ at redshift $z = 1.0$ and convergence $\kappa(\theta, z')$ at redshift $z' = 2.0$, when δ is drawn from a lognormal distribution and κ computed by density LoS integration (darker regions have higher probability densities), estimated using $\sim 12.5 \times 10^6$ realisations. The dashed blue contours represent the two-dimensional multivariate lognormal PDF whose means, covariances and skewnesses are the same as those for the former PDF. If these two PDFs were the same, the contours would overlap. *Right panel:* this contour plot shows the difference between the two PDFs in the left panel (density LoS integration PDF minus lognormal PDF). The red regions have negative values while blue regions have positive values.

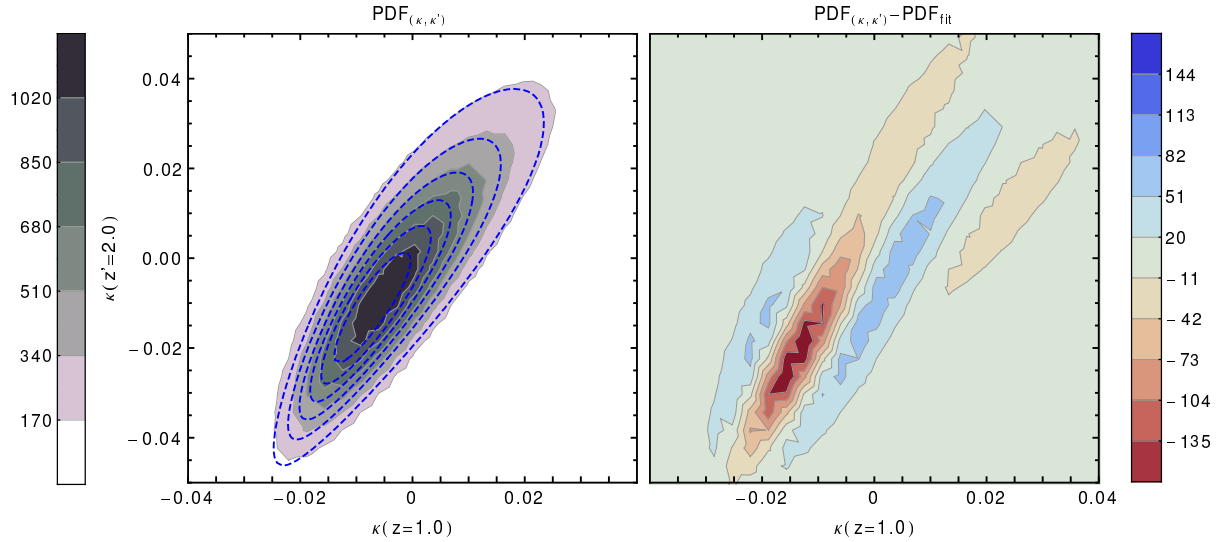


Figure 12. Same as Fig. 11 but for two convergences computed by density LoS integration (along the same LoS) for sources at redshifts $z = 1.0$ and $z' = 2.0$.

4 THE LINE-OF-SIGHT INTEGRATION SOLUTION

The limitations for simulating correlated density and convergence presented in Sec. 3.1 can be circumvented in three ways. First, by simulating Gaussian instead of lognormal fields; as explained in Sec. 2.2, Gaussian variables are less limited in terms of valid covariance matrices than lognormal ones (as a trade-off, however, one loses the skewness and minimum boundary of the lognormal distribution). A second option is to distort the input power spectra so they produce positive-definite covariance matrices; once you have a valid covariance matrix for the associated Gaussian multipoles, the lognormal simulation can proceed without further issues. This is acceptable if the application intended for the simulations does not require the input $C(\ell)$ s to be linked to a particular cosmologi-

cal model or if the fractional changes applied to the input $C(\ell)$ s are within the precision tolerance. The third option is to generate an only-density lognormal simulation and obtain the convergence by performing an approximated LoS integration through a weighted Riemann sum of the simulated densities in the redshift bins; as presented in Sec. 3.1, density realisations are not plagued by lognormal limitations.

As shown in Figs. 9 to 12, such integration leads to a convergence field that follows a distribution different from the lognormal (although fairly similar). To test if such a convergence field follows the expected statistics, we created 1000 full-sky simulations of the density field in 40 contiguous redshift bins of width $\Delta z = 0.05$, spanning the range $0.025 < z < 2.025$, and computed the con-

z	κ_{\min}	κ_{\max}	m	s	t	γ	κ_0	p -value
0.525	-0.0164	0.105	-0.001458	0.00690	31.034	-1.383	0.040	0.002
0.575	-0.0191	0.121	-0.001516	0.00764	27.047	-1.663	0.053	0.103
0.625	-0.0213	0.117	-0.001566	0.00837	23.974	-1.998	0.069	0.052
0.675	-0.0234	0.111	-0.001609	0.00907	21.405	-2.400	0.089	0.281
0.725	-0.0257	0.123	-0.001647	0.00976	19.019	-2.748	0.111	0.425
0.775	-0.0286	0.132	-0.001680	0.01044	17.368	-3.346	0.145	0.385
0.825	-0.0315	0.125	-0.001708	0.01109	15.864	-4.070	0.188	0.231
0.875	-0.0342	0.141	-0.001734	0.01173	14.419	-4.766	0.235	0.270
0.925	-0.0361	0.139	-0.001755	0.01235	13.412	-6.209	0.322	0.648
0.975	-0.0382	0.137	-0.001772	0.01295	12.596	-8.798	0.476	0.715
1.025	-0.0409	0.147	-0.001786	0.01354	12.060	-16.499	0.922	0.074
1.075	-0.0435	0.154	-0.001799	0.01411	11.249	-30.820	1.807	0.389
1.125	-0.0461	0.141	-0.001812	0.01466	10.055	-30.820	1.935	0.172
1.175	-0.0484	0.144	-0.001823	0.01520	9.048	-30.820	2.064	0.859
1.225	-0.0501	0.151	-0.001832	0.01573	8.194	-30.820	2.196	0.161
1.275	-0.0517	0.152	-0.001841	0.01624	7.490	-30.820	2.324	0.399
1.325	-0.0535	0.151	-0.001846	0.01673	6.670	-30.820	2.460	0.356
1.375	-0.0560	0.153	-0.001851	0.01722	6.045	-30.820	2.594	0.068
1.425	-0.0584	0.172	-0.001857	0.01769	5.447	-30.820	2.726	0.098
1.475	-0.0603	0.171	-0.001859	0.01814	4.913	-30.820	2.861	0.263
1.525	-0.0617	0.161	-0.001862	0.01859	4.426	-30.820	2.998	0.060
1.575	-0.0637	0.173	-0.001863	0.01902	3.955	-30.820	3.133	0.012
1.625	-0.0652	0.155	-0.001864	0.01945	3.642	-30.820	3.272	0.001
1.675	-0.0663	0.181	-0.001864	0.01986	3.103	-30.820	3.407	0.050
1.725	-0.0672	0.186	-0.001865	0.02027	2.721	-30.820	3.543	3.7×10^{-4}
1.775	-0.0685	0.169	-0.001864	0.02066	2.393	-30.820	3.681	0.003
1.825	-0.0704	0.178	-0.001864	0.02105	2.124	-30.820	3.818	0.001
1.875	-0.0725	0.179	-0.001863	0.02143	1.798	-30.820	3.954	2.2×10^{-4}
1.925	-0.0747	0.166	-0.001862	0.02180	1.416	-30.820	4.088	0.017
1.975	-0.0768	0.191	-0.001862	0.02216	0.972	-30.820	4.221	0.058
2.025	-0.0788	0.187	-0.001860	0.02251	0.509	-30.820	4.358	0.022

Table 3. Fit to the marginal distribution of the convergence obtained by LoS integration of the lognormal density. The columns are, from left to right: the sources' redshift z , the minimum and maximum convergences used in the fit, the five $f_{\text{ABC}}(\kappa)$ parameters and the fit p -value. From $z = 1.075$ onwards, γ is fixed to the best-fitting parameter for that redshift to avoid numerical instabilities.

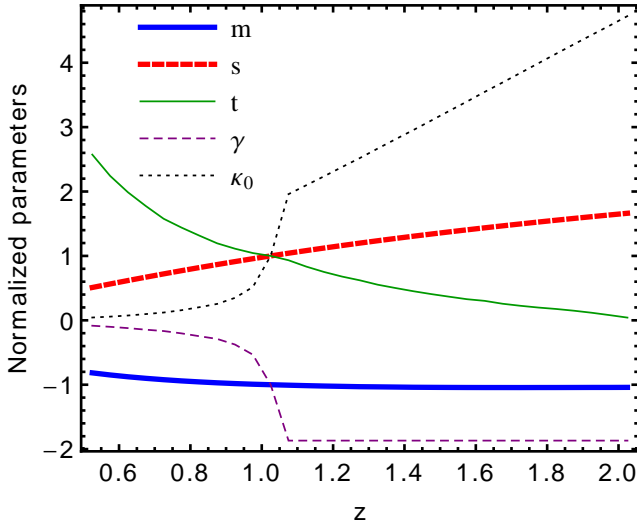


Figure 13. Best-fitting parameters from Table 3, normalised by their absolute values at $z = 1.025$.

vergence by approximating the integral in Eq. 22 by a Riemann sum. We approximated the continuous density contrast $\delta(\theta, z)$ by its average inside redshift bins $\bar{\delta}(\theta, z_i)$ (which already is the CLASS

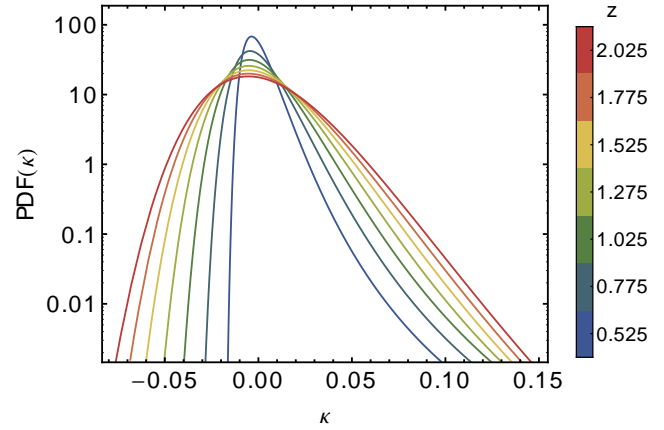


Figure 14. Best-fitting $f_{\text{ABC}}(\kappa)$ distributions for the convergence obtained from lognormal density LoS integration, for various redshifts. As the redshift of the sources increases, the distribution gets closer to a Gaussian.

output) and the kernel $K(z, z_s)$ by its average inside the same bins $\bar{K}(z_i, z_s)$:

$$\kappa(\theta, z_s) \simeq \sum_i \bar{K}(z_i, z_s) \bar{\delta}(\theta, z_i) \Delta z_i. \quad (31)$$

We then recovered the power spectra from the convergence field computed as above and compared with the CLASS output. It is worth noting that the effects of such approximation can be predicted from $C^{\delta(z)\delta(z')}(\ell)$, the spectra for the average density contrasts $\bar{\delta}$ at redshift bins centred at z and z' , computed by CLASS. The power spectra expected for convergence κ at redshifts z_s and z'_s , and for density contrast $\bar{\delta}$ at redshift z and convergence at redshift z_s , are:

$$\tilde{C}^{\kappa(z_s)\kappa(z'_s)}(\ell) = \sum_i \sum_j \bar{K}(z_i, z_s) \bar{K}(z_j, z'_s) C^{\bar{\delta}(z_i)\bar{\delta}(z_j)}(\ell) \Delta z_i \Delta z_j, \quad (32)$$

$$\tilde{C}^{\bar{\delta}(z)\kappa(z_s)}(\ell) = \sum_i \bar{K}(z_i, z_s) C^{\bar{\delta}(z)\bar{\delta}(z_i)}(\ell) \Delta z_i. \quad (33)$$

A representative set of the results of this comparison is shown in Fig. 15. All analysed power spectra in the range $0.5 < z < 2.025$ and for $\ell \gtrsim 100$ succeed in reproducing the theoretical ones computed by CLASS with a 3% precision (we did not study the spectra for which the density is at higher redshift than the convergence since these are very small); in fact, the convergence–convergence power spectra in this redshift range all agree to CLASS $C^{\kappa\kappa}(\ell)$ s at 1% all the way down to $\ell \sim 20$ or better.

One thing that can be seen in Fig. 15 is that the agreement is worse at lower redshifts. This happens for two reasons: first, the number of density bins used to compute the convergence is smaller (10 for $z = 0.5$ against 40 for $z = 2.0$), rendering a coarser integral approximation; secondly, the truncation of the integral at $z = 0.025$ instead of at $z = 0$ (CLASS could not compute power spectra for bins centred at $z < 0.05$) is more relevant for lower redshifts, thus producing a systematic power loss. We can also see that the agreement is worse for lower multipoles. This happens because $C^{\delta(z)\delta(z')}(\ell)$ is more sharply peaked in this case and therefore the approximation of the integral by a sum is less accurate.

Another aspect worth noting in Fig. 15 is that the density–convergence power spectra are well recovered with a precision better than 1% down to $\ell \sim 10$ in most cases, the exception being when the density redshift bin is very close to the convergence redshift. This might not be an issue for high redshifts where, as shown by the large error bars, such measurements are quite difficult to be performed, but at lower redshifts it can present up to 3% deviations at $\ell \gtrsim 60$ and even larger ones at lower multipoles. Part of the problem can be accounted by the precision of CLASS $C(\ell)$ s: the power spectra $C^{\delta(z)\delta(z')}(\ell)$ used to simulate the density fields have to be well tuned with the convergence spectra used as $C_{\text{true}}(\ell)$. Moreover, the outcome of Eq. 33 refers to the average density inside a top-hat bin and the convergence at an exact redshift z_s , something that cannot be computed by CLASS; the comparison was made with the convergence in a top-hat redshift bin of width $\Delta z = 0.002$ centred at the border of the last density bin used in the integration.

Finally, Fig. 15 shows that the theoretical prediction from Eqs. 32 and 33, depicted by the red lines, works excellently. Thus, if the intended application for the simulations requires convergence fields that accurately follow a fiducial $C(\ell)$ but otherwise can deviate from a specific cosmological model, this method can be very powerful since comparisons can be made to these predictions.

5 FLASK CODE DESCRIPTION

5.1 Overview

The purpose of FLASK is to generate two- or three-dimensional random realisations of astrophysical fields such as matter, arbitrary tracer densities, weak lensing convergence and shear in a correlated way, that is, all simulated fields (e.g. multiple tracers and weak lensing) are connected through the same realisation and therefore follow the expected internal cross-correlations provided as input. According to the user's choice, the realisations can follow either a multivariate Gaussian distribution or a multivariate lognormal distribution in which case each field's one-dimensional marginal distribution is lognormal (note that mixed Gaussian and lognormal marginals can also be generated since the Gaussian case can be described as a special lognormal case when the field's skewness is zero). In comparison to the Gaussian, the lognormal distribution is a better approximation to matter and tracer densities and to the lensing convergence; it also does not lead to nonphysical values such as negative densities.

Another FLASK feature is that the realisations are created on the full sky using spherical geometry: the observer is positioned in the centre of the simulation and the universe is discretized along the LoS into spherical shells around the observer of arbitrary thickness (like an onion) with the slices being themselves discretized into a fixed number of aligned pixels (see Fig. 16). Such geometry allows for easy implementation of effects such as evolution with redshift, redshift space distortions and survey selection functions. Moreover, it is well matched for upcoming large area surveys than box-shaped simulations.

The goal of FLASK is to create the full-sky lognormal simulations quickly. Its power spectrum realisation approach and its implementation in C++ using OPENMP allows it to generate, for instance, 40 full-sky redshift slices of correlated convergence and density fields, each with ~ 50 million pixels ($N_{\text{side}} = 2048$, which permits analysis to be made up to multipoles around $\ell \simeq 4000$), in 10 minutes using a 16 core computer. This redshift and angular resolution suffices to create full-size mock catalogues for photometric large-scale structure surveys, such as those planned by *Euclid* and LSST, with cosmological signals known to the per-cent level. Another relevant aspect of the approach adopted by FLASK is that the statistical properties of the fields (i.e. their power spectra and distributions) are defined *a priori* and obeyed by construction apart from discretization and truncation inaccuracies that vanish in the limit of infinite resolution. This can be an important advantage for certain applications like verifying power spectrum and correlation function estimators, evaluating their covariance matrices and testing the effects of systematics and statistical fluctuations on these measurements. On the down side, the fact that all statistical properties are set by the multivariate lognormal model means that the code cannot produce anything different from that (although there is the option to model the convergence as a sum of correlated lognormal variables): three-point functions, for instance, are bound to behave according to the model and might not give a realistic representation of the data; for such applications one might need N -body simulations (e.g. following Fosalba et al. 2008).

After generating the fields [which might already include redshift space distortions, magnification bias and intrinsic alignments if these were included in the input power spectra – see Kirk et al. (2010); Challinor & Lewis (2011); Blas et al. (2011); Dio et al. (2013)], FLASK can: apply survey selection functions (that can be different for different tracers and can be separable or not into radial and angular parts), Poisson sample tracers from their density

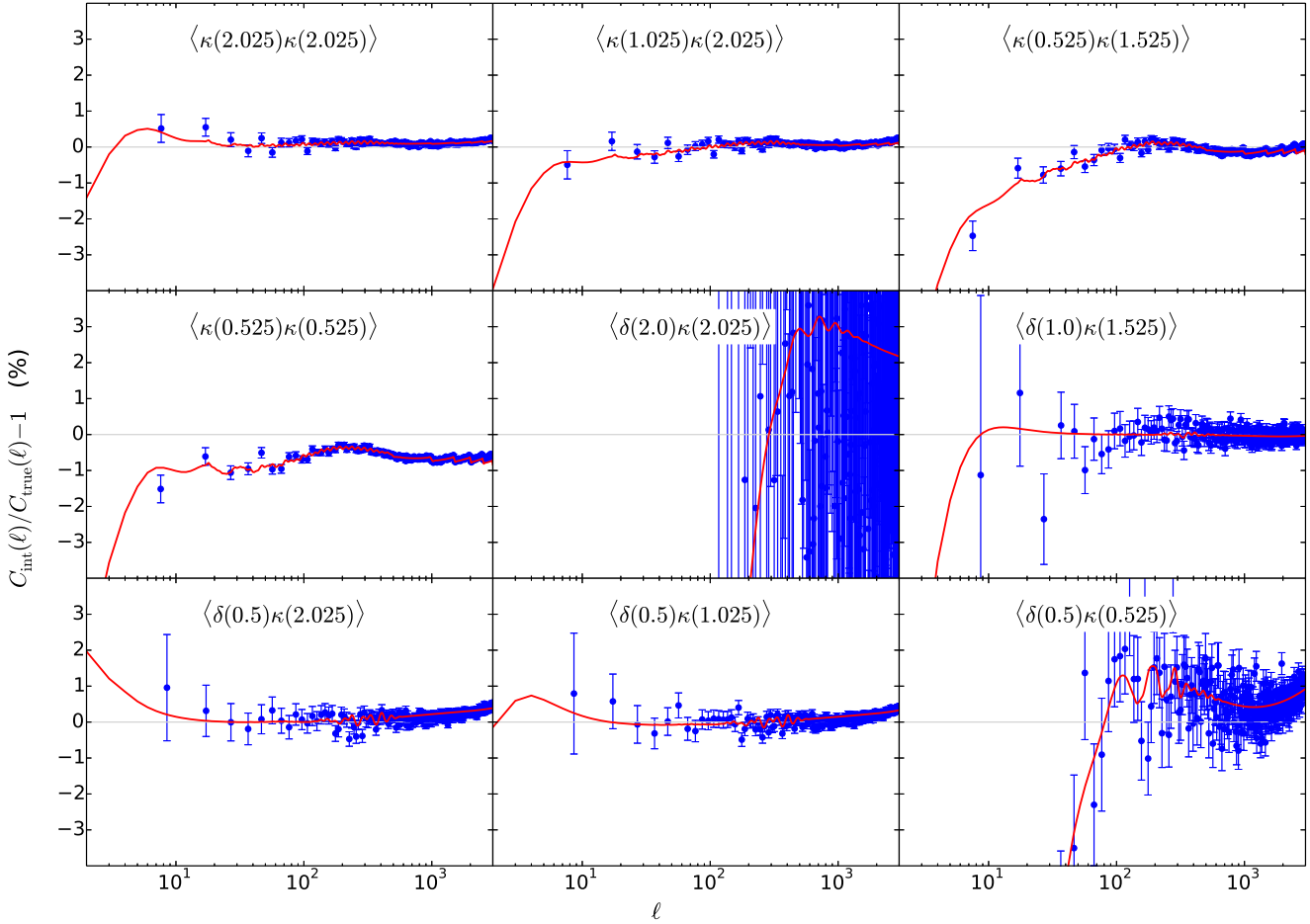


Figure 15. Fractional difference between the angular power spectra for the convergence computed as a LoS Riemann sum of the simulated density, $C_{\text{int}}(\ell)$, and the one computed by CLASS, $C_{\text{true}}(\ell)$. The red curves show the theoretical expectation of the results, given by Eqs. 32 and 33, and the blue data points show the average of 1000 power spectra recovered from independent density field realisations, averaged inside $10\text{-}\ell$ bins. The error bars show the error on the mean. The first four subplots show the results for convergence–convergence power spectra while the last five subplots show the results for the density–convergence power spectra. The density was simulated in 40 redshift bins of width $\Delta z = 0.05$, and results were analysed for the bins centred at 0.5, 1.0, 1.5 and 2.0. The convergence was computed for sources at redshifts 0.525, 1.025, 1.525 and 2.025.

fields, compute shear and ellipticities and introduce Gaussian noise in the latter. The final results can be output in the form of a source catalogue. Appendix B presents an example of FLASK usage and output.

5.2 Details

5.2.1 Input

FLASK is run by calling it on a terminal followed by a configuration file containing all specifications needed – which can also be overridden through the command line. Besides a keyword setting the type of simulation to be performed – Gaussian, lognormal or homogeneous (i.e. Poisson sampling from density fields containing no structure) –, two inputs described in the configuration file fully specify all statistical properties of the fields: a file containing a table of fields’ means, shifts and redshift ranges and a set of angular auto and cross power spectra $C_{\text{ln}}^{ij}(\ell)$ for all fields at all redshift slices that must be provided by the user (the indices i and j cycle both through fields and redshift slices). These $C_{\text{ln}}^{ij}(\ell)$ s can be calculated by public codes such as CLASS (Blas et al. 2011; Dio et al. 2013),

by CAMB SOURCES (Challinor & Lewis 2011) or by any other routine. In order to fix the fields’ properties, all cross-correlations have to be specified [there is an option to treat missing $C_{\text{ln}}^{ij}(\ell)$ s as zero, that is, the field/redshift i is uncorrelated with the field/redshift j]. For instance, N_f fields described in N_z redshift slices require a total of $N_f N_z (N_f N_z + 1)/2$ $C_{\text{ln}}^{ij}(\ell)$ s to be fully specified. Each field can be simulated in a different number of redshift slices which can have different ranges as well.

5.2.2 Obtaining the associated Gaussian power spectra

The process of simulating a lognormal field involves first generating a Gaussian one and exponentiating it afterwards. To associate the statistical properties of the Gaussian to the lognormal field using Eq. 7 we assume statistical homogeneity and isotropy and that the field value at each point in space is a random variable. Since Eq. 7 is local, the correlation functions of the lognormal and Gaussian fields $\xi_{\text{ln}}^{ij}(\theta)$ and $\xi_{ij}^g(\theta)$ have the same form as that equation:

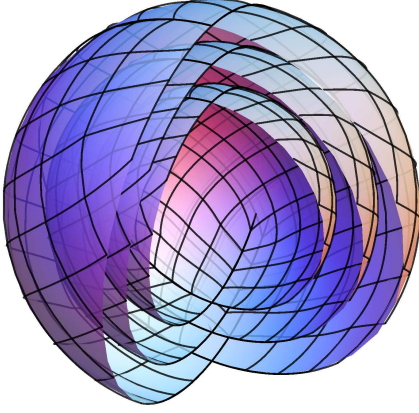


Figure 16. Example of discretization of space used in FLASK (a quarter of the concentric spherical surfaces were removed to ease visualisation). The observer is located in the centre of the spheres. The surfaces represent the cells' boundaries in the radial direction and the black lines represent their angular boundaries. In this example there are two radial slices, each with 192 cells of same angular size. The radial slices can have arbitrary thickness while the angular part in all slices follows the same HEALPIX pixelization scheme.

$$\xi_g^{ij}(\theta) = \ln \left[\frac{\xi_{\ln}^{ij}(\theta)}{\alpha_i \alpha_j} + 1 \right]. \quad (34)$$

Even though $\xi_g^{ij}(\theta)$ specify a covariance matrix for the field in all points in space that could be used to generate correlated Gaussian variables, in practice this approach is impossible due to its size. A more economical approach is to go to harmonic space since isotropy leads to independent multipoles. The relations between the correlation function $\xi^{ij}(\theta)$ and the power spectrum $C^{ij}(\ell)$ are given by Eqs. 19 and 20. To obtain the angular power spectra $C_g^{ij}(\ell)$ for the Gaussian fields we: (i) transform the input $C_{\ln}^{ij}(\ell)$ to real space using Eq. 20; (ii) compute $\xi_g^{ij}(\theta)$ using Eq. 34; and (iii) go back to harmonic space with Eq. 19. In practice the transformations to and from harmonic space are performed using the discrete Legendre transform routines implemented in S2KIT¹³ (Kostelec et al. 2000). For Gaussian realisations, this transformation is skipped and the input power spectra are directly used to generate the multipoles; in other words, in this case FLASK simply sets $C_g^{ij}(\ell) = C_{\ln}^{ij}(\ell)$.

It is interesting and important to note that since the relation between lognormal and Gaussian fields $X_i(\hat{\theta})$ and $Z_i(\hat{\theta})$ is local in real space, it is non-local in harmonic space, i.e. each multipole of the lognormal field depends on a mix of the Gaussian multipoles. This can be demonstrated through a series expansion of the exponential:

$$X_i(\hat{\theta}) = e^{Z_i(\hat{\theta})} - \lambda_i \simeq 1 - \lambda_i + Z_i(\hat{\theta}) + \frac{Z_i^2(\hat{\theta})}{2} + \dots \quad (35)$$

We can expand $X_i(\hat{\theta})$ and $Z_i(\hat{\theta})$ in spherical harmonics:

¹³ <http://www.cs.dartmouth.edu/~geelong/sphere>

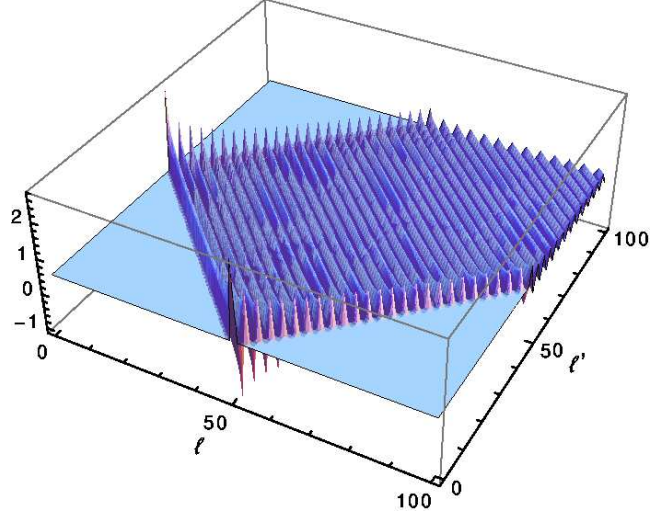


Figure 17. Value of the first Wigner 3-j symbol in Eq. 37 for $L = 50$. This serves as an indication that Gaussian multipoles at $l > L$ contribute to the lognormal multipole. The structure shown is similar for higher L as well.

$$a(\hat{\theta}) = \sum_{l,m} a_{lm} Y_{lm}(\hat{\theta}) \quad (36)$$

and show that the contribution $X_{i,L,M}^{(2)}$ of the last written term on the right-hand side of Eq. 35 to the multipole $X_{i,L,M}^{\ln}$ of the lognormal field is:

$$\begin{aligned} X_{i,L,M}^{(2)} = & \sum_{l,m,l',m'} \frac{Z_{i,lm} Z_{i,l'm'}}{2} \int Y_{lm}(\hat{\theta}) Y_{l'm'}(\hat{\theta}) Y_{LM}^*(\hat{\theta}) d^2 \hat{\theta} = \\ & \sum_{l,m,l',m'} \frac{Z_{i,lm} Z_{i,l'm'}}{2} \sqrt{\frac{(2l+1)(2l'+1)(2L+1)}{4\pi}} \times \\ & (-1)^M \begin{pmatrix} l & l' & L \\ 0 & 0 & 0 \end{pmatrix} \begin{pmatrix} l & l' & L \\ m & m' & -M \end{pmatrix}, \quad (37) \end{aligned}$$

where $\begin{pmatrix} l_1 & l_2 & l_3 \\ m_1 & m_2 & m_3 \end{pmatrix}$ are Wigner 3-j symbols. These can be non-zero if $m_1 + m_2 + m_3 = 0$ and $|l_1 - l_2| \leq l_3 \leq l_1 + l_2$, which shows that $X_{i,L,M}^{(2)}$ can get contributions from $Z_{i,lm}$ with $l > L$ (see Fig. 17). The practical consequence of such non-locality is that if one wants to accurately simulate lognormal fields up to a bandlimit L_{\max} , it is necessary to generate Gaussian multipoles up to $l_{\max} > L_{\max}$. This fact is a general characteristic of lognormal fields and does not depend on the chosen transform (e.g. an analogous relation exists for Fourier transforms). Fig. 18 shows an example of this effect for the density contrast angular power spectra at redshift $z = 0.2$ for a Λ CDM model; the larger the non-Gaussianity, the larger the effect.

Lastly, the necessity of truncating the series in Eq. 20 at a finite ℓ introduces a hard bandlimit that translates into oscillations in $\xi^{ij}(\theta)$. These oscillations can be minimised by increasing the series range to higher ℓ and/or by introducing a high- ℓ suppression in $C^{ij}(\ell)$. FLASK has the option of applying exponential suppressions and those that result from convolving the field with Gaussian and/or Healpix pixel window functions.

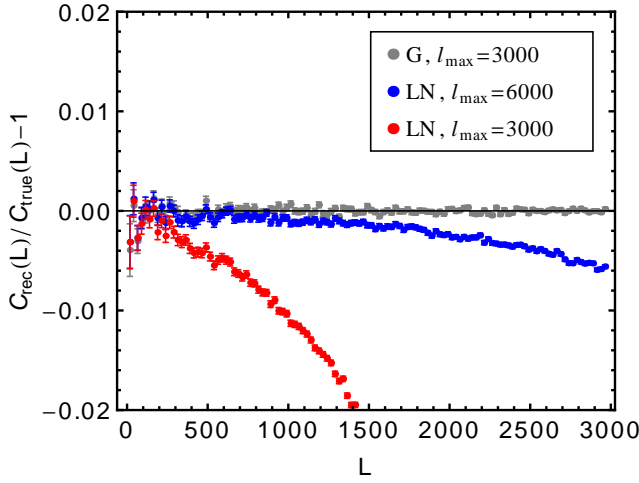


Figure 18. Fractional difference between true angular power spectrum and the average of recoveries from 400 full-sky realisations, averaged inside 25- ℓ bins. The data points represent: Gaussian realisation with bandlimit $l_{\max} = 3000$ (grey) and lognormal realisations with associated Gaussian field bandlimits $l_{\max} = 6000$ (blue) and $l_{\max} = 3000$ (red). In this example, the simulation of the Gaussian field up to $l_{\max} = 6000$ is enough to get a precision of less than one per cent for the lognormal field power spectrum up to $L = 3000$. The error bars represent the error on the mean.

5.2.3 Generating correlated multipoles

The statistical isotropy of the simulations allows for each multipole $Z_{i,\ell m}$ with different ℓ and m indices to be generated independently. However, multipoles with the same ℓ and m but from different fields and/or redshift slices (hence different i indices) might be correlated. To generate such correlated Gaussian multipoles, we construct a covariance matrix for each multipole ℓ using the values of $C_g^{ij}(\ell)$ as elements of that matrix. We then apply a Cholesky decomposition [using the GNU Scientific Library (GSL) routine¹⁴] to the covariance matrix $\mathbf{C}_g(\ell)$:

$$C_g^{ij}(\ell) = \sum_k T_{ik}(\ell) T_{jk}(\ell), \quad (38)$$

where $\mathbf{T}(\ell)$ are lower triangular matrices which can be used to generate the correlated Gaussian multipoles from a set of standard (zero mean and unit variance) independent Gaussian variables $Z_{k,\ell m}^0$:

$$Z_{i,\ell m} = \sum_k T_{ik}(\ell) Z_{k,\ell m}^0. \quad (39)$$

The computation of the expected value $\langle Z_{i,\ell m} Z_{j,\ell' m'} \rangle$ shows that $Z_{i,\ell m}$ indeed follow $C_g^{ij}(\ell) \delta_{\ell\ell'} \delta_{mm'}$ where δ_{ab} are Kronecker deltas.

Non-positive-definite matrices (those with non-positive eigenvalues) cannot be decomposed as in Eq. 38; in fact, these are invalid covariance matrices in the sense that no set of variables can possibly have such covariances. Even though one can start with a set of $C_{\ln}^{ij}(\ell)$ s that, as expected, leads to a positive-definite matrix $\mathbf{C}_{\ln}(\ell)$ for each ℓ , the matrix $\mathbf{C}_g(\ell)$ obtained as described in Sec. 5.2.2 might not be positive-definite for two reasons: numerical errors and the fundamental limitation described in Sec. 2.3. While numerical

errors are small enough such that a fractional change of $\lesssim 10^{-4}$ in the $C_{\ln}^{ij}(\ell)$ s (a negligible change for most cosmological applications) is sufficient to solve the problem, the second reason might need significantly larger fractional changes; moreover, it cannot be overcome with more accurate computations or different simulation methods since it is intrinsic to lognormal variables.

For generic fields, FLASK can fix this problem by distorting the covariance matrices $\mathbf{C}_g(\ell)$ as little as possible so they become positive-definite. Unfortunately, there are different ways to quantify the distance between two matrices; therefore, two methods are provided: one is guaranteed to minimise the Frobenius norm (quadratic sum of the matrix elements) of the difference between the regularised matrix and the original one (Higham 1988); and the other aims at applying the smallest fractional change possible to the matrix. The first one is quite fast since it simply performs an eigen-decomposition of the matrix $[\mathbf{C}_g(\ell) = \mathbf{Q}(\ell) \mathbf{\Lambda}(\ell) \mathbf{Q}(\ell)^{-1}]$, where $\mathbf{Q}(\ell)$ is a matrix whose columns are eigenvectors of $\mathbf{C}_g(\ell)$ and $\mathbf{\Lambda}(\ell)$ is a diagonal matrix formed by $\mathbf{C}_g(\ell)$ eigenvalues] and then sets the negative eigenvalues to zero (or close to zero for numerical reasons).

The second method is an iterative one and therefore takes more time. For an $N \times N$ matrix, it tries to obtain positive eigenvalues by applying successive fractional changes to its elements in the $N \times N$ -dimensional direction of greatest change for the negative eigenvalues. In other words, it computes the gradient of the sum of the negative eigenvalues as a function of all matrix elements and follows it until all eigenvalues are positive. Although there is no rigorous proof that this method reaches the minimum fractional change required to make the matrix positive-definite, this is what can be expected from following the negative eigenvalues gradient and it indeed performs better in this sense than alternative methods like simply adding small values to the matrix diagonal or like the first one presented (however it is possible that the larger fractional changes produced by the first method might only affect uninteresting $C_g^{ij}(\ell)$ s with very low power).

5.2.4 Map generation

Once the multipoles $Z_{i,\ell m}$ for the zero mean Gaussian fields are generated, we build HEALPIX maps $Z_i(\hat{\theta})$ from them using the ALM2MAP HEALPIX function.

If the goal is to generate Gaussian fields, no extra step is needed. However, if one wants to generate lognormal fields $X_i(\hat{\theta})$, we have to apply the following local transformation to the Gaussian maps $Z_i(\hat{\theta})$:

$$X_i(\hat{\theta}) = e^{\mu_i} e^{Z_i(\hat{\theta})} - \lambda_i, \quad (40)$$

$$e^{\mu_i} = (\langle X_i \rangle + \lambda_i) e^{-\sigma_i^2/2}, \quad (41)$$

where σ_i^2 is the variance of the Gaussian field $Z_i(\hat{\theta})$, given by

$$\sigma_i^2 = \sum_{\ell=\ell_{\min}}^{\ell_{\max}} \frac{2\ell+1}{4\pi} C_g^{ii}(\ell). \quad (42)$$

Although e^{μ_i} can also be directly related to the lognormal field variance (Eq. 13) – which in turn is related to $C_{\ln}^{ii}(\ell)$ by an equation identical to Eq. 42 – the fact that in practice we generate Gaussian multipoles in the strict range $\ell_{\min} \leq \ell \leq \ell_{\max}$ means that the lognormal field multipole range is not well defined (see Sec. 5.2.2), making such calculation more difficult.

¹⁴ <http://www.gnu.org/software/gsl>

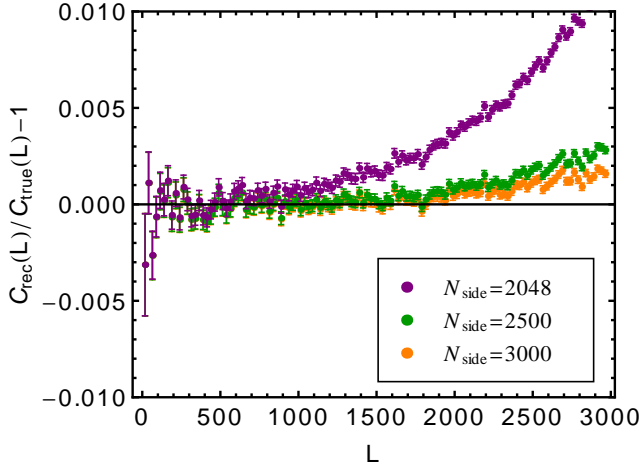


Figure 19. Fractional difference between the average of lognormal field power spectra measured from 400 realizations of lognormal field maps and the original power spectrum, averaged inside 25- ℓ bins, for different map resolutions: $N_{\text{side}} = 2048$ (purple), $N_{\text{side}} = 2500$ (green) and $N_{\text{side}} = 3000$ (orange). All maps were generated by exponentiating Gaussian fields band-limited to $\ell_{\text{max}} = 7000$. The error bars represent the error on the mean.

The multipole mixing referred to in Sec. 5.2.2 also introduces the issue that while the Gaussian field is band limited to ℓ_{max} , the exponentiation via Eq. 40 excites modes beyond ℓ_{max} as Eq. 37 exemplifies. Such an increase in the bandlimit is analogous to what happens in trigonometric identities such as $\cos^2(\omega\theta) = 1/2 + \cos(2\omega\theta)/2$. This leads to the need of higher HEALPIX map resolutions than would be expected from the Gaussian field bandlimit to avoid aliasing effects. An example of this is shown in Fig. 19, where we compare the original power spectrum with the ones reconstructed from full-sky lognormal maps with different resolutions, all generated from an associated Gaussian field with bandlimit $\ell_{\text{max}} = 7000$. While the resolutions as small as $N_{\text{side}} = \ell_{\text{max}}/4$ are enough for the Gaussian field, we need to go to $N_{\text{side}} \simeq \ell_{\text{max}}/3$ to get to one per cent precision on the lognormal field. Together with the need to simulate the Gaussian field up to higher multipoles than required, this makes lognormal field simulations more costly in terms of memory than Gaussian fields.

Since homogeneity and isotropy of the fields on a spherical shell manifest themselves in the harmonic space as multipole independence $\langle a_{i,\ell m} a_{j,\ell' m'} \rangle = C^{ij}(\ell) \delta_{\ell\ell'} \delta_{mm'}$, one might ask if the multipole mixing that happens during exponentiation can break these symmetries by introducing correlations between different multipoles. Fortunately, this cannot happen since the transformation from a Gaussian to a lognormal field is local and homogeneous in real space over the spherical shell and as such cannot introduce a preferential location or direction. Nevertheless we verified the independence of the lognormal field multipoles by realising them 2000 times in the range $2 < \ell < 100$ and $0 \leq m \leq \ell$ [since the field is real, $a_{\ell,-m} = (-1)^m a_{\ell,m}^*$] and measuring all their correlations [a total of $5148 \times (5148+1)/2 = 13,253,526$ elements]. The off-diagonal terms ($\langle a_{\ell m} a_{\ell' m'} \rangle$ with $\ell \neq \ell'$ and $m \neq m'$) only show random statistical fluctuations smaller than 5 per cent. This isotropy conservation means that the exponentiation process is a rotation (and possibly an isotropic dilation) in harmonic space.

5.2.5 Density line-of-sight integration

If a set of density maps were generated in contiguous redshift slices (of arbitrary thickness), FLASK can use them to compute a convergence field for sources located at each slice boundary up to the last one at redshift z_{last} using the approximation described in Sec. 4. For these convergence fields to be accurate, the redshift slices should be reasonably thin and cover the redshift range $0 \lesssim z < z_{\text{last}}$. The power spectra expected to be followed by these convergence fields (e.g. the red curves in Fig. 15) can be computed by an auxiliary routine in FLASK.

5.2.6 Shear computation

Weak gravitational lensing caused by matter distributed along the LoS will distort the images of distant galaxies by bending the path travelled by the photons coming from them: if a photon comes from the true angular position $\hat{\beta}$, it might be observed at a different position $\hat{\theta}$. The distortion in the image can be described to first order by the partial derivatives of $\hat{\beta}$ with respect to $\hat{\theta}$ components, $\partial\hat{\beta}_i/\partial\hat{\theta}_j$, which is parametrized by the three parameters κ (convergence), γ_1 and γ_2 (shear components; Bartelmann & Schneider 2001):

$$\frac{\partial\hat{\beta}_i}{\partial\hat{\theta}_j} = \begin{pmatrix} 1 - \kappa - \gamma_1 & -\gamma_2 \\ -\gamma_2 & 1 - \kappa + \gamma_1 \end{pmatrix}. \quad (43)$$

Both the shear distortion and the flux and apparent size magnification described by the convergence are caused by the same intervening matter, and the shear can be deduced from the convergence, whose angular power spectra should be provided by the user as input if one wants to generate shear fields (alternatively, the convergence can be computed from the density fields as presented in the previous section). The shear can be described as an expansion over spin-2 spherical harmonics $_{\pm 2}Y_{\ell m}(\hat{\theta})$ (Zaldarriaga & Seljak 1997, as in HEALPIX convention):

$$\pm\gamma(\hat{\theta}) = \gamma_1(\hat{\theta}) \pm i\gamma_2(\hat{\theta}) = \sum_{\ell m} \gamma_{\ell m} \pm 2Y_{\ell m}(\hat{\theta}). \quad (44)$$

According to Hu (2000), on the full sky the harmonic multipoles $\gamma_{\ell m}$ are related to the convergence ones $\kappa_{\ell m}$ by:

$$\gamma_{\ell m} = -\sqrt{\frac{(\ell+2)(\ell-1)}{\ell(\ell+1)}} \kappa_{\ell m}. \quad (45)$$

Therefore the process of computing the shear $\gamma_1(\hat{\theta})$ and $\gamma_2(\hat{\theta})$ involves first computing $\gamma_{\ell m}$ from $\kappa_{\ell m}$. For Gaussian realisations, the latter are obtained directly as described in Sec. 5.2.3, whereas for lognormal realisations they have to be extracted from the lognormal HEALPIX maps computed as described in Sec. 5.2.4. We then use the HEALPIX function ALM2MAP_SPIN to transform the shear E and B mode multipoles, $E_{\ell m}$ and $B_{\ell m}$, into $\gamma_1(\hat{\theta})$ and $\gamma_2(\hat{\theta})$. According to the HEALPIX manual, $E_{\ell m} = -\gamma_{\ell m}$ and $B_{\ell m} = 0$.

In the lognormal case, we must obtain $\kappa_{\ell m}$ from the maps using the MAP2ALM_ITER function (with one iteration), and this process can introduce noise in the shears if the map resolution is too low compared to the shear bandwidth ℓ_{max} . To avoid that, we recommend $N_{\text{side}} \sim \ell_{\text{max}}$.

5.2.7 Noise and selection effects

Once the tracer density contrast fields $\delta_i(\hat{\theta})$ are available, FLASK can apply the survey selection function $\bar{n}_i(\hat{\theta})$ (i.e. the expected observed density if the universe had no structure, provided by the user) to $\delta_i(\hat{\theta})$ to get the expected observed density, used as the mean value of a Poisson distribution from which we will draw the actual observed tracer density $n_i(\hat{\theta})$:

$$n_i(\hat{\theta}) = \text{Poisson}\{\bar{n}_i(\hat{\theta})[1 + \delta_i(\hat{\theta})]\}. \quad (46)$$

The user has to provide a selection function for each one of the tracers (if there is more than one) and each selection function can be separable or not into angular and radial directions. For separable selection functions, the user must supply: a file describing the radial part as a table containing the redshifts and the expected number of observed tracers of that type per unit arcmin² per unit redshift; and a HEALPIX map describing the fractions of this number that are observed at each angular coordinate. The final selection function is the product of these two. In the case of non-separable selection functions, a different HEALPIX map must be provided for each redshift slice, each one containing the expected number of observed tracers per unit arcmin² per unit redshift.

5.2.8 Catalogue building and output

All quantities computed in the previous sections (from angular correlation functions $\xi^{ij}(\theta)$ in Sec. 5.2.2 to HEALPIX maps of $n_i(\hat{\theta})$ in Sec. 5.2.7) can be written to output files on request, along with other quantities like the $C_{\text{in}}^{ij}(\ell)$ s obtained from the regularised $\mathbf{C}_g(\ell)$ matrices described in Sec. 5.2.3 and the $C_{\text{in}}^{ij}(\ell)$ s recovered from full-sky maps described in Sec. 5.2.4. The final FLASK product and output is a catalogue of observed tracers that might contain the following columns, according to user request: angular position (using polar and azimuth angles or right ascension and declination, given in radians or degrees), redshift, tracer type, convergence, shear components, ellipticity components (see Eq. 47), and a few bookkeeping numbers.

Up to the catalogue creation step, all tracers inside a cell are associated with the cell's angular position (given by the HEALPIX map pixel centre position) and redshift (given by its redshift slice). During the catalogue creation process, each tracer in the cell gets a random angular position homogeneously sampled within the pixel boundaries and a random redshift sampled within its redshift slice according to an interpolation of the selection function such that, even if the simulated redshift slices are thick, the resulting radial distribution of tracers is smooth (no structure will be generated inside the slices, though). The ellipticities $\epsilon = \epsilon_1 + i\epsilon_2$ are computed using the equation (Bartelmann & Schneider 2001):

$$\epsilon = \begin{cases} \frac{\epsilon_s + g}{1 + g^* \epsilon_s}, & |g| \leq 1; \\ \frac{1 + g \epsilon_s^*}{\epsilon_s^* + g^*}, & |g| > 1; \end{cases} \quad (47)$$

where $g \equiv +\gamma/(1 - \kappa)$ is the reduced shear and $\epsilon_s = \epsilon_{s,1} + i\epsilon_{s,2}$ is the source intrinsic ellipticity, randomly drawn from a Gaussian distribution with variance set by the user. For introducing intrinsic alignment in the simulations, these have to be specified via the input power spectra.

6 SUMMARY AND CONCLUSIONS

The lognormal modelling of large-scale structure (LSS) fields is an important tool for validating LSS data analysis, estimating covariance matrices and studying impact of noise, selection and systematic effects on the data. Current and future photometric LSS surveys require this modelling to be performed jointly for many observables, on the full sky and over a large redshift interval. In this paper we explained some of the obstacles faced by this task and described how the modelling can be performed accurately. We also presented a public code that can create such simulations for a wide range of field combinations.

We showed in Sec. 2.2 that lognormal variables cannot attain certain correlations or covariance matrices that would be, for instance, accessible to Gaussian variables. Although this is a known fact in the field of statistics, it remained unnoticed by the astrophysics community given it does not manifest itself when modelling density and convergence fields in an independent way, as was done so far. We then showed in Sec. 2.3 that these limitations are propagated to the harmonic space in a similar but smoothed out way, and that as a consequence of such limitations the covariance matrix of the associated Gaussian variables becomes non-positive-definite.

In Sec. 3.1 we presented a way of quantifying the amount of “non-positive-definiteness” by computing the fractional change required to make the covariance matrix positive-definite and showed that, when modelling both density and convergence as a multivariate lognormal field, the change required is much larger than the expected numerical errors, demonstrating that they are caused by intrinsic limitations in the model; therefore, better implementations of the same simulation process will not circumvent the problem. We verified in Sec. 3.2 that the multivariate lognormal model for both density and convergence is internally inconsistent as the density lognormality assumption leads to a non-lognormal distribution for the convergence. This is likely the reason why the lognormal model fails to result in valid covariance matrices for the associated Gaussian variables when modelling both fields together.

We must therefore look for alternative methods if we want to create correlated random realisations of density and lensing. In this paper, two solutions were proposed: distorting the density and convergence auto and cross power spectra (Sec. 3.1); or using non-lognormal convergence marginal distributions (Sec. 4), for which we provided a fitting function in Sec. 3.4. Given that the lognormal model works well for the density and that the convergence can be obtained from the former by line-of-sight (LoS) integration, changing the shape of the convergence distribution to that of a sum of correlated lognormals allows both fields to be jointly modelled (see Fig. 15). Another (less attractive) possibility is to use the multivariate Gaussian model for creating realisations of the joint density and convergence fields: since the sum of Gaussian variables is also Gaussian, this model does not include the internal inconsistencies seen above. This alternative, however, has been shown to lead to underestimations of the convergence measurements covariance matrix (Hilbert et al. 2011).

Other bold possibilities would be to: (a) try different marginal distributions for the convergence [e.g. Das & Ostriker (2006); Schuhmann et al. (2016) or different approximations to the sum of lognormal variables] or even for the density fields; or (b) try different copulas (note that the multivariate lognormal distribution corresponds to the Gaussian copula with lognormal marginals; Nelsen 2006). Compared to the multivariate lognormal distribution, both have the disadvantage that specifying the fields' statistical proper-

ties – e.g. the power spectra – might not be as straightforward as in the lognormal case (it might not even be analytically possible). Moreover, a different copula would still lead to the same limits in the fields’ correlations described in Sec. 2.2 given that they are limited by the Fréchet–Hoeffding bounds.

When modelling the convergence as a lognormal field, its shift parameter λ (an additional parameter that specifies the minimum value of the lognormal distribution $X_{\min} = -\lambda$) is not fixed by the convergence power spectra and has to be determined somehow. Given that the true convergence field is not lognormal, different methods of estimating the shift parameter return different values (see Table 2) that confer to the model different characteristics when compared to the real distribution. Using Eqs. 11 and 28, we provided a way to specify it directly from theory, without relying on ray-tracing simulations. In comparison to the method by Taruya et al. (2002), our method is more complex but it is built to reproduce the convergence skewness while the method of Taruya et al. (2002) reproduces the minimum value observed in a finite sample. Given the arbitrariness on how λ is set when modelling the convergence distribution, there is no reason to expect it to match the minimum value of the convergence (i.e. the one obtained in an empty LoS, κ_{empty}) unless the fit is specifically built to reproduce this value in detriment of other properties. This conclusion leads us to question the common interpretation that the difference between $-\lambda$ and κ_{empty} is an indication that there are no empty lines of sight in the Universe.

Finally, we presented in Sec. 5 the public code FLASK¹⁵ which is able to simulate an arbitrary number of correlated lognormal and Gaussian fields including multiple tracer densities, convergence and CMB radiation once their statistics are specified by an input power spectra set which can be computed by CLASS or CAMB SOURCES, for instance. In case the lognormal limitations prevent the realisation of the fields, FLASK can overcome these limitations by distorting the input power spectra or by computing the convergence through a density LoS integration. Effects such as redshift space distortions, evolution, galaxy intrinsic alignments and arbitrary biases can be introduced by inscribing their effects in the power spectra, while selection functions and noise can be applied by FLASK itself. The code adopts a tomographic approach on the full curved sky, thus making it ideal for large-area photometric surveys like DES, *Euclid*, J-PAS, LSST and *WISE*.

7 ACKNOWLEDGEMENTS

The authors would like to thank Dr. Sreekumar Balan and Prof. Laerte Sodré Jr. for useful discussions. This work was made possible by the financial support of FAPESP Brazilian funding agency. BJ acknowledges support by an STFC Ernest Rutherford Fellowship, grant reference ST/J004421/1.

APPENDIX A: SUM OF CORRELATED LOGNORMAL VARIABLES

We are interested in the first three central moments of the distribution of Y which is a sum of lognormal variables X_i weighted by a_i :

$$Y = \sum_i a_i X_i. \quad (\text{A1})$$

¹⁵ <http://www.astro.iag.usp.br/~flask>

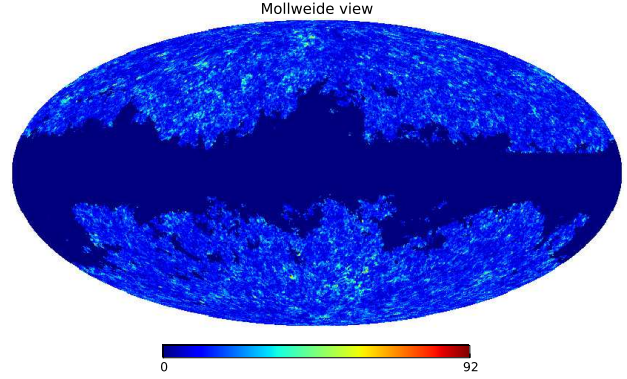


Figure B1. A Mollweide projection of a galaxy counts HEALPIX map produced by FLASK, simulating the *WISE* survey.

They can all be easily computed from the one-, two- and three-point functions presented in Sec. 2.1:

$$\langle Y \rangle = \sum_i a_i \langle X_i \rangle, \quad (\text{A2})$$

$$\langle Y^2 \rangle - \langle Y \rangle^2 = \sum_{ij} a_i a_j \xi_{\text{ln}}^{ij}, \quad (\text{A3})$$

$$\langle (Y - \langle Y \rangle)^3 \rangle = \sum_{ijk} a_i a_j a_k \zeta_{\text{ln}}^{ijk}, \quad (\text{A4})$$

APPENDIX B: FLASK USAGE EXAMPLE

FLASK is executed in the command line by calling it together with a configuration file:

```
flask sim-01.config
```

The configuration file specifies all settings using keywords followed by a colon. For instance, `RNDSEED: 1243` specifies the random number generator seed and `MAP_OUT: data/kappa-map-01.dat` specifies an output file for a table of field values at all angular positions. FLASK comes with an example configuration file that describes all keywords; these are also explained in detail in FLASK’s documentation.

All settings can be overridden by providing new values in the command line, e.g.:

```
flask example.config RNDSEED: 334 MAP_OUT:
./map-002.dat
```

Among many possible outputs, the code can produce HEALPIX maps of the generated fields. Fig. B1 shows a FLASK simulation of the *WISE* survey (under a Λ CDM model), consisting of galaxy counts following the survey selection function, including the Milky Way angular mask.

REFERENCES

- Alonso D., Salvador A. I., Sánchez F. J., Bilicki M., García-Bellido J., Sánchez E., 2015, *MNRAS*, 449, 670
- Bartelmann M., Schneider P., 2001, *Physics Reports*, 340, 291
- Benítez N., et al., 2014, arXiv pre-print, 1403.5237
- Bernardeau F., Kofman L., 1995, *ApJ*, 443, 479
- Beutler F., et al., 2014, *MNRAS*, 443, 1065

- Blas D., Lesgourgues J., Tram T., 2011, *J. Cosmol. Astropart. Phys.*, 1107, 034
- Challinor A., Lewis A., 2011, *Phys. Rev. D*, 84, 043516
- Chiang C.-T., et al., 2013, *J. Cosmol. Astropart. Phys.*, 2013, 030
- Coles P., Jones B., 1991, *MNRAS*, 248, 248
- Crow E. L., Shimizu K., 1988, *Lognormal distributions: theory and applications*. Marcel Dekker, Inc., New York, USA
- Das S., Ostriker J. P., 2006, *ApJ*, 645, 1
- Denuit M., Dhaene J., 2003, *Belgian Actuarial Bulletin*, 3, 22
- DES Collaboration 2005, *arXiv astro-ph*, 0510346
- Dio E. D., Montanari F., Lesgourgues J., Durrer R., 2013, *J. Cosmol. Astropart. Phys.*, 1311, 044
- Durrer R., 2008, *The Cosmic Microwave Background*. Cambridge University Press, Cambridge, UK
- Fenton L. F., 1960, *IRE Transactions on Communication Systems*, CS-8, 57
- Fosalba P., Gaztañaga E., Castander F. J., Manera M., 2008, *MNRAS*, 391, 435
- Higham N. J., 1988, *Linear Algebra and its Applications*, 103, 103
- Hilbert S., Hartlap J., Schneider P., 2011, *A&A*, 536, A85
- Hu W., 2000, *Phys. Rev. D*, 62, 043007
- Joachimi B., Taylor A. N., Kiessling A., 2011, *MNRAS*, 418, 145
- Kainulainen K., Marra V., 2011, *Phys. Rev. D*, 83, 023009
- Kayo I., Taruya A., Suto Y., 2001, *ApJ*, 561, 22
- Kirk D., Bridle S., Schneider M., 2010, *MNRAS*, 408, 1502
- Kofman L., Bertschinger E., Gelb J. M., Nusser A., Dekel A., 1994, *ApJ*, 420, 44
- Kostelec P., Maslen D. K., Rockmore D. N., Healy D. J., 2000, *J. Computational Physics*, 162, 514
- Lam C. L. J., Le-Ngoc T., 2007, *Wireless personal communications*, 41, 179
- Li X., Wu Z., Chakravarthy V. D., Wu Z., 2011, *IEEE Transactions on Vehicular Technology*, 60, 4040
- LSST collaboration 2009, *arXiv pre-print*, 0912.0201
- Lumb D., Duvet L., Laurijs R., Plate M. T., Sanz I. E., Criado G. S., 2009, *Proceedings of the SPIE*, 7436, 743604
- Nelsen R. B., 2006, *An Introduction to Copulas*. Springer, New York, USA
- Neyrinck M., 2011, *ApJ*, 742, 91
- Peebles P. J. E., 1993, *Principles of physical cosmology*. Princeton University Press, Princeton, USA
- Schuhmann R. L., Joachimi B., Peiris H. V., 2016, *MNRAS*, 459, 1916
- Schwartz S. C., Yeh Y. S., 1982, *Bell System Technological Journal*, 61, 1441
- Seo H.-J., Sato M., Takada M., Dodelson S., 2012, *ApJ*, 748, 57
- Smith R. E., et al., 2003, *MNRAS*, 341, 1311
- Takahashi R., Sato M., Nishimichi T., Taruya A., Oguri M., 2012, *ApJ*, 761, 152
- Taruya A., Takada M., Hamana T., Kayo I., Futamase T., 2002, *ApJ*, 571, 638
- Wright E. L., 2010, *ApJ*, 140, 1868
- Zaldarriaga M., Seljak U., 1997, *Phys. Rev. D*, 55, 1830